Integrated design optimization of a novel electrically-driven helicopter ECS using low-GWP refrigerants as working fluid

Ascione, F.; Giuffré, A.; Colonna, P.; De Servi, C. M.

DOI
10.1016/j.ijrefrig.2025.06.015

Publication date
2025

Document Version
Final published version

Published in
International Journal of Refrigeration

Citation (APA)
Ascione, F., Giuffré, A., Colonna, P., & De Servi, C. M. (2025). Integrated design optimization of a novel electrically-driven helicopter ECS using low-GWP refrigerants as working fluid. *International Journal of Refrigeration*, *178*, 379-395. https://doi.org/10.1016/j.ijrefrig.2025.06.015

International Journal of Refrigeration 178 (2025) 379–395

Contents lists available at ScienceDirect

International Journal of Refrigeration

journal homepage: www.elsevier.com/locate/ijrefrig

INSTITUT INTERNATIONAL DU FROID
INTERNATIONAL INSTITUTE OF REFRIGERATION

Integrated design optimization of a novel electrically-driven helicopter ECS using low-GWP refrigerants as working fluid

F. Ascione [a], A. Giuffré [a], P. Colonna [a], C.M. De Servi [a,b,*]

[a] *Propulsion and Power, Delft University of Technology, Kluyverweg 1, Delft, 2629 HS, The Netherlands*
[b] *Energy Technology Unit, VITO, Beretang 200, BE-2400, Mol, Belgium*

ARTICLE INFO

Keywords:
Environmental control system
Vapour compression cycle
High-speed centrifugal compressor
Haloolefins
Low-GWP refrigerants
Multi-objective optimization

ABSTRACT

The Environmental Control System (ECS) is the main utilizer of non-propulsive power among the aircraft subsystems. Onboard helicopters, the ECS is based on the Vapour Compression Cycle (VCC) concept, and the standard refrigerant is R-134a. The objective of this study is to evaluate the impact of replacing the conventional scroll compressor with a high-speed centrifugal compressor operating with a low-GWP refrigerant as the prime mover of the VCC system. The case study is the ECS of a large helicopter and the sizing operating condition is that of the helicopter on the ground on a hot and humid day. The working fluids identified as potential alternatives to R-134a are the haloolefins R-1233zd(E), R-1234ze(Z), R-1224yd(Z) and R-1336mzz(Z). An integrated design optimization method has been employed to simultaneously account for the design of the VCC system, its main components, and the selection of the working fluid. The model of the VCC system has been coded with the acausal Modelica language. The design of the high-speed compressor has been performed with an in-house program validated with experimental data. The objectives of the optimization are the maximization of the Coefficient of Performance (COP) and the minimization of the system weight. The results show that the use of haloolefins in place of R-134a allows the design of lighter and more efficient VCC systems. In particular, the refrigerant R-1234ze(Z) enables the identification of an optimal design point featuring a 12% increase in COP and a 26% reduction in weight.

1. Introduction

One of the goals stated in the European Green Deal Proposal is the 90% reduction in transport emissions to achieve climate neutrality by 2050 (Zaporozhets et al., 2021). In the transport sector, aviation is identified as the second largest source of Greenhouse Gas (GhG) emissions after road transport, accounting for almost 14% of the total (Buticchi et al., 2022). The Advisory Council for Aeronautics Research in Europe (ACARE) published the Strategic Research and Innovation Agenda (SRIA) FlightPath 2050 to address the aviation industry emissions and to call for alternative and more sustainable technologies. The objective is to achieve a 75% reduction of CO_2 emissions per passenger-km and a 90% decrease of NO_x emissions to face the growing air transportation demand observed in the last few decades (European Commission, 2011). The need for more sustainable aviation has oriented significant research efforts towards aircraft and rotorcraft electrification. The idea is to improve fuel efficiency by electrifying actuation systems, the ice protection system, the environmental control system, and fuel pumping. The Environmental Control System (ECS) is responsible for cabin air pressurization and passengers thermal comfort. It is one of the main users of non-propulsive energy (AIR1168/8, 2011), accounting for 3%–5% of the total energy consumption (Bender, 2019).

The idea underpinning this work is that the efficiency and the environmental footprint of the ECS can be improved by resorting to an electrically-driven Vapour Compression Cycle (VCC) system. The case study is the design of the ECS for a large passenger helicopter. Traditionally, the ECS of such vehicles already features a VCC system operating with R-134a. However, the temperature lift in the refrigeration loop is provided by a mechanically-driven scroll compressor. In this context, the novelties of the proposed ECS configuration are the use of an electrically-driven high-speed centrifugal compressor and a low-Global Warming Potential (GWP[1]) refrigerant. Centrifugal compressors are more compact and are characterized by higher performance than scroll compressors, whose isentropic efficiency does not

---

* Corresponding author at: Propulsion and Power, Delft University of Technology, Kluyverweg 1, Delft, 2629 HS, The Netherlands.
E-mail addresses: f.ascione@tudelft.nl (F. Ascione), a.giuffre@tudelft.nl (A. Giuffré), p.colonna@tudelft.nl (P. Colonna), c.m.deservi@tudelft.nl (C.M. De Servi).

[1] The authors refer to the GWP_{100} index, which provides an estimate of the environmental impact of a substance with respect to that of the CO_2 over a time horizon of 100 years.

https://doi.org/10.1016/j.ijrefrig.2025.06.015
Received 31 July 2024; Received in revised form 9 June 2025; Accepted 13 June 2025

Nomenclature

Acronyms

ACARE	Advisory Council for Aeronautics Research in Europe
ALFT	Atmospheric lifetime
ASF	Augmented Scalarization Function
CAD	Computer-Aided Design
COP	Coefficient Of Performance
CV	Control Volume
ECS	Environmental Control System
ECU	Electronic Control Unit
F-gas	Fluorinated greenhouse gases
FV	Finite Volume
GhG	Greenhouse Gas
GWP	Global Warming Potential
HCFO	Hydrochlorofluoro-olefin
HEX	Heat Exchanger
HFC	Hydrofluorocarbon
HFO	Hydrofluoroolefin
MB	Moving Boundaries
MEA	More Electric Aircraft
MGB	Motor Gear Box
MOO	Multi-objective optimization
NBP	Normal Boiling Point (°C)
ODP	Ozone Depletion Potential
SRIA	Strategic Research and Innovation Agenda
TFA	Trifluoracetic acid
VCC	Vapour Compression Cycle

Greek Symbol

α	Absolute angle (°)
β	Compactness factor (–), Compression ratio (–)
δ	Thickness (m)
ϵ	Effectiveness (–)
η	Efficiency (–)
Ω	Rotational speed (rpm)
Φ_t	Swallowing capacity (–)
Ψ	Loading coefficient (–)
ρ	Density (kg m^{-3})
σ	Molecular complexity (–)
Θ	Louver angle (°)

Subscripts

1	Compressor impeller inlet
2	Compressor impeller outlet
3	Compressor diffuser outlet
air	Air flow stream
ax	Axial
bl	Compressor impeller blades
C	Critical property
cb	Cabin air stream
cold	Cold flow stream
compr	Compressor
cond	Conduction
env	Environment
eva	Evaporator
fan	Fan
fresh	Fresh air stream
h	Impeller hub
hot	Hot flow stream
hub	Compressor hub
in	Inlet section
inj	Injected
int	Intermediate
is	Isentropic
max	Maximum value
min	Minimum value
r	Reduced property
ram	Ram air stream
rec	Recirculated air stream
refr	Refrigerant
s	Compressor shroud
t	Total thermodynamic state
tt	Total-to-total
w	Relative velocity

Roman Symbol

$\dot{m}$	Mass flow rate (kg s^{-1})
$\dot{Q}$	Heat transfer rate (W)
$\dot{W}$	Power (W)
ρ	Density (kg m^{-3})
A	Heat transfer area (m^2)
a	Speed of sound (m s^{-1})
C	Thermal capacity (W K^{-1})
C_r	Thermal capacity ratio (–)
c_p	Specific heat capacity at constant pressure (J (kg K)$^{-1}$)
D	Depth (m), Diameter (m)
F	Force (N)
f	Objective function
g	Inequality constraint
H	Height (m), Blade height (m)
h	Specific enthalpy (J kg^{-1})
k	Shape factor (–)
L	Length (m)
L_l	Louver length (m)
L_p	Louver pitch (m)
M	Molar mass (g mol^{-1})
N	Number (–)
NTU	Number of Thermal Units (–)
p	Pressure (Pa)
R	Gas constant (J (kg K)$^{-1}$), Radius (m)
s	Specific entropy (J (kg K)$^{-1}$)
T	Temperature (°C)
U	Impeller blade speed (m s^{-1})
V	Volume (m^3)
v	Flow velocity (m s^{-1})
W	Width (m)
x	Vapour quality (–), Design variable

Table 1

List of the main thermodynamic properties of the working fluids tested for the helicopter ECS optimization (ANSI/ASHRAE Standard 34, 2022; Lemmon et al., 2018).

ASHRAE designation	R-134a	R-1233zd(E)	R-1224yd(Z)	R-1234ze(Z)	R-1336mzz(Z)
Chemical formula	CH_2FCF_3	$CF_3CH{=}CHCl$	$CF_3CF{=}CHCl$	$CF_3CH{=}CFH$	$CF_3CH{=}CHCF_3$
Category	HFC	HCFO	HCFO	HFO	HFO
Safety class	A1	A1	A1	A2L	A1
GWP	1300	1	<1	1	2
ODP	0	0	0	0	0
ALFT	13.4 years	26 days	21 days	16.4 days	22 days
NBP/°C	–26	18.2	14.6	9.7	33.4
σ[a]/–	–1.10	3.92	4.91	1.50	9.24
M/g mol^{-1}	102.0	130.5	148.5	114.0	164.1
T_C/°C	101	166.5	155.5	150.1	171.3
p_C/bar	40.6	36.2	33.4	35.3	29.0
$\rho_{x=1\|_{T=0\ ^\circ C}}$/kg m^{-3}	14.4	2.8	3.8	3.6	1.8

[a] The values of molecular complexity are estimated assuming that saturated vapour properties approximate those of the ideal gas, namely: $\sigma \approx \frac{C_p}{0.7R} - \frac{\log 10}{0.49}\frac{7}{3}(\omega + 1)$ (Invernizzi, 2013).

exceed 70% (Hundy et al., 2016). Moreover, centrifugal compressors can be operated with gas bearings, thus avoiding oil contamination in the refrigerant loop.

The global warming emergency has urged legislative bodies to establish regulations about the use of fluorinated greenhouse gases (F-gas) (Heath, 2017; European Commission, 2022). The Kigali Amendment to the Montréal Protocol (Heath, 2017) states the gradual phasing out of high-GWP hydrofluorocarbons (HFCs) from the market by encouraging the use of alternative substances, known as *fourth-generation refrigerants*, i.e., natural refrigerants, haloolefins, and HFC-HFO blends. Several recent studies deal with the transition to low-GWP refrigerants for VCC systems by investigating the use of haloolefins, i.e., hydrofluoroolefins (HFOs) and hydrochlorofluoro-olefins (HCFOs), envisioned as the next-generation refrigerants, in light of their low GWP, which can be even smaller than that of CO_2 (McLinden et al., 2020). However, none of these studies consider aircraft or rotorcraft ECS as the application. Among the investigated applications, air conditioning aboard passenger vehicles is arguably the application most similar to that of interest in this work, apart from the aspect of mass production. It is thus no coincidence that helicopter VCC systems are often made of components originally developed for automotive air conditioning. In this regard, Mohanraj and Abraham (2022) provided an exhaustive review of refrigerants considered as alternative options to the state-of-the-art R-134a working fluid for automotive air conditioning systems. In particular, among the HFOs, R-1234yf and R-1234ze are indicated as the two most suitable drop-in substitutes of R-134a, thanks to their similar thermodynamic properties. In general, their use leads to a slight performance decrease (COP and cooling capacity) of the VCC system. Moreover, they require certain safety measures given their, though mild, flammability. The same considerations are reported by Prabakaran et al. (2023). Mohanraj and Abraham (2022) also point out that, during the atmospheric degradation of haloolefins, trifluoroacetic acid (TFA), a substance that is harmful to aquatic life, is produced. However, the molar yield of the degradation of haloolefins in the atmosphere can be rather small, as low as 2% in the case of R-1233zd(E) (Andersen et al., 2018; Arpagaus et al., 2019; Arpagaus and Bertsch, 2021). The only exception is R-1224yd(Z) whose TFA molar yield is 97% (Arpagaus and Bertsch, 2021). Though recently European regulation (ECHA, 2023) proposed a gradual ban on per- and polyfluoroalkyl substances (PFAS) due to environmental and health concerns, haloolefins continue to be the best alternative to high-GWP refrigerants in vapour compression cycle (VCC) systems in aviation. The reason is that current safety regulations (EASA CS-25.863, 2016; MIL-STD-882E, 2023) make the use of hydrocarbons, which are currently the only environmentally-friendly substitute for synthetic refrigerants, impractical in refrigeration systems aboard aircraft and rotorcraft.

Few research studies have addressed the design of centrifugal compressors for VCC systems operating with low-GWP refrigerants (Giuffré et al., 2022a,b). If working fluid selection is included in the system analysis, investigations are limited to studies considering just two working fluids belonging to the class of the HFOs, i.e., R-1234yf and R-1234ze(E), treated as drop-in replacements of R-134a (Molés et al., 2014; Yataganbaba et al., 2015).

To deal with the call for new sustainable solutions in the air conditioning and refrigeration sector, the current work focuses on analysing the impact of low-GWP refrigerants on the optimal design of a VCC system for the ECS of a large passenger helicopter. Ascione et al. (2021) performed an exploratory study by testing a large number of low-GWP refrigerants for the same ECS configuration considered here. From the analysis of the cycle thermodynamic performance, the authors identified four haloolefins as potential alternatives to the state-of-the-art R-134a, namely R-1233zd(E), R-1224yd(Z), R-1234ze(Z) and R-1336mzz(Z). The aim of this study is to expand the previous work by investigating the effect of these low-GWP refrigerants on the optimal design of the VCC-based ECS of a large passenger helicopter. In the same fashion as in the work by Ascione et al. (2024), the design optimization of the VCC system is carried out with an in-house integrated design framework, capable of simultaneously optimizing the thermodynamic cycle and the preliminary design of the main components, i.e., the heat exchangers (HEXs) and the high-speed centrifugal compressor. Another difference with the aforementioned work is the approach utilized for the centrifugal compressor design and the simulation of the combined system.

The article is structured as follows. First, a review of the thermodynamic properties of the selected low-GWP refrigerants is presented. Then, the VCC system layout for large helicopters is described. Next, the integrated design optimization method is illustrated. Thereafter, the multi-objective optimization problem is introduced, by specifying the design space, objective functions, and constraints. The results of the optimization are then presented, together with the analysis of the effect of the working fluid on the design of the main system components. Finally, the main outcomes of the study are summarized and an overview of future work is also provided.

2. Working fluids

With reference to Table 1, the main thermodynamic properties and characteristics of the selected haloolefins in comparison to those of R-134a, can be summarized as (i) higher molecular complexity σ; (ii) larger molar mass M; (iii) higher critical temperature and lower critical pressure; (iv) significantly lower saturated vapour density. The molecular complexity σ, defined as Angelino and Invernizzi (1988)

$$\begin{aligned}\sigma &= \frac{T_C}{R}\left[\frac{ds}{dT}\right]_{x=1,T_r=0.7} \\ &= \frac{T_C}{R}\left[\frac{c_p}{T} - \left(\frac{\partial V}{\partial T}\right)_p \frac{\mathrm{d}p}{\mathrm{d}T}\right]_{x=1,T_r=0.7},\end{aligned} \tag{1}$$

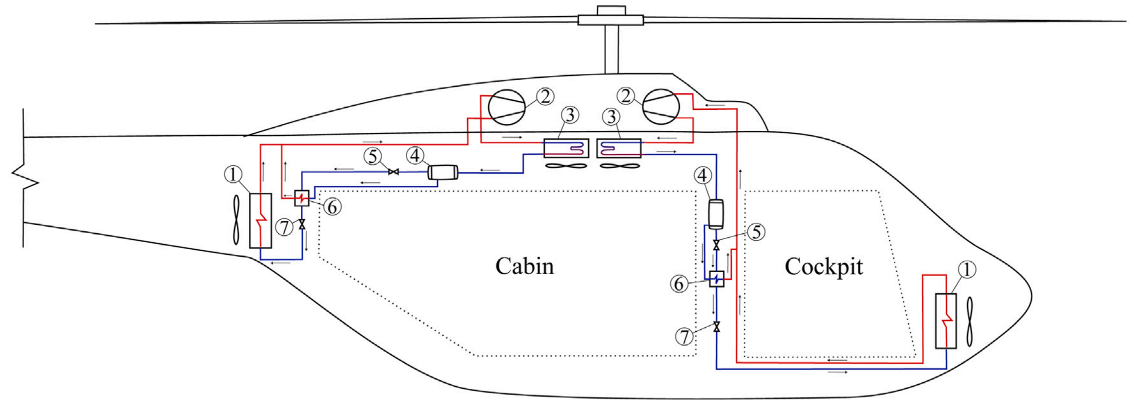

Fig. 1. Arrangement of the Environmental Control System's components in the helicopter: (1) Evaporator, (2) Compressor, (3) Condenser unit, (4) Liquid tank, (5) Expansion valve, (6) Intercooler, (7) Expansion valve. After (Ascione et al., 2024).

is a semi-empirically derived fluid thermodynamic property related to the complexity of fluid molecules. Complexity refers to the number of atoms in a molecule and their arrangement. Substances with high molecular complexity are characterized by large specific heat capacity (c_p) since the large number of atoms in a molecule increases their degree of freedom in terms of rotational and vibrational modes (Hodnebrog et al., 2020). Therefore, at macroscopic level, σ is proportional to the slope of the saturated vapour line in the T-s plane (calculated at the reduced temperature of 0.7), and to the critical temperature. Both quantities increase with the complexity of the fluid molecule. With reference to Eq. (1) and Fig. 2, substances known as dry fluids (fluids whose isentropically expanding vapour remains dry) are characterized by large and positive values of σ. These classes of compounds are characterized by large critical temperature and low critical pressure in opposite fashion to those of fluids featuring low molecular complexity, i.e., wet fluids. As shown in Fig. 2, given the design temperature specifications of the considered small-capacity VCC system, the thermodynamic losses associated with vapour superheating along the compression process are limited if the working fluid is made of complex molecules. Given that the latent specific enthalpy of vaporization of the considered fluids at the considered saturation temperatures is similar, therefore mass flow rates are also similar, and that the selected haloolefins also feature low values of saturated vapour density, the resulting values of volume flow rate affect the size of the components, leading to larger flow passages to reduce the flow velocity and avoid high friction losses. In the case of VCC-based ECS for helicopters adopting high-speed centrifugal compressors, the use of low-density refrigerants allows to design of an impeller wheel with sufficiently large diameter and non-excessive rotational speed. The fluid molecular complexity also affects the speed of sound, which is low in the case of fluids made of complex molecules. This therefore makes the design of turbomachinery components more challenging, due to the likely occurrence of transonic flow through the cascades, leading to a reduction of both isentropic efficiency and choke margin.

The refrigerants selected for this study are non-flammable, with the exception of R-1234ze(Z) (see Table 1). R-1234ze(Z) has a safety classification of A2L, which means that the fluid flammability is low as well as the flame propagation speed. In aviation, flammability is an important safety concern, and systems operating with A2L refrigerants are practically excluded from certification given the complex risk mitigation solutions that the use of these working fluids currently requires. In the refrigeration sector, current regulations are promoting the adoption of sustainable refrigerants, albeit flammable, such as hydrocarbons and some haloolefins. Therefore, novel technological solutions are being developed to ease the operation with flammable refrigerants through advanced safety systems and protocols (IEC 60335-2-40:2022, 2022; IEC 60335-2-89:2019, 2023). In this framework, the adoption of refrigerants with mild flammability for aircraft and rotorcraft VCC-based ECS might become viable in a near future, paving the way for the adoption of hydrocarbons.

3. Environmental control system

The selected test case is the optimal design of the ECS of a large helicopter, thus capable of transporting 20 passengers and 2 pilots. The ECS is composed of two sub-systems: one for cabin heating and another for cooling. Due to the relatively low flying altitudes, hence the low power requirement, the cabin air is heated simply by mixing hot air bled from the engine with fresh air. The cabin air cooling system is based on VCC technology, and it consists of two separate loops, one for cockpit cooling and the other for cabin cooling. This research focuses on the integrated design optimization of the rotorcraft cooling loop, hereinafter indicated simply as ECS. The system configuration features two compression stages and an intercooler (or economizer). Its novelty lies in the adoption of a twin-stage high-speed electrically-driven centrifugal compressor, in place of the commonly used scroll compressor. Such design choice allows for higher efficiency, lower weight, and improved compactness. Furthermore, being electrically-driven, the compressor can be placed far from the Main Gear Box (MGB), which is typically installed in the upper part of the vehicle. This enables the use of a shorter hose connecting the evaporator outlet with the compressor suction port. This piping operates at the lowest system pressure level, hence a decrease of the pressure drop in this section may beneficially influence the system efficiency, especially when operating with low-density refrigerants. Each refrigeration loop features an evaporator. The cockpit evaporator is situated beneath the floor at the front of the helicopter, while the cabin evaporator is typically placed towards the rear of the helicopter. Fig. 1 shows a schematic representation of the typical installation layout of the VCC system aboard helicopters.

To guarantee passengers comfort, the ARP292 (2014) standard specifies a target mass flow rate of air for each evaporator, i.e., 4.5 g s^{-1} of fresh air for the cabin and 5.6 g s^{-1} for the cockpit, keeping the air humidity below 65%. Since the flight altitude is relatively low, cabin air pressurization is unnecessary. This allows for a significantly higher ratio of recirculated to fresh air compared to a typical aircraft ECS. The condenser unit consists of three HEXs in series on the air side and in parallel on the refrigerant side. Both condenser and evaporator have independent air intakes and electrically-driven fans. The prime-mover of the system is a twin-stage centrifugal compressor. Two compression stages are needed to meet the required temperature lift. The two compressor wheels are mounted in a back-to-back configuration to balance their axial thrust, thus allowing for the use of gas bearings. An intercooler is installed to further reduce the temperature of the condensed refrigerant upstream of the expansion valve. In this way,

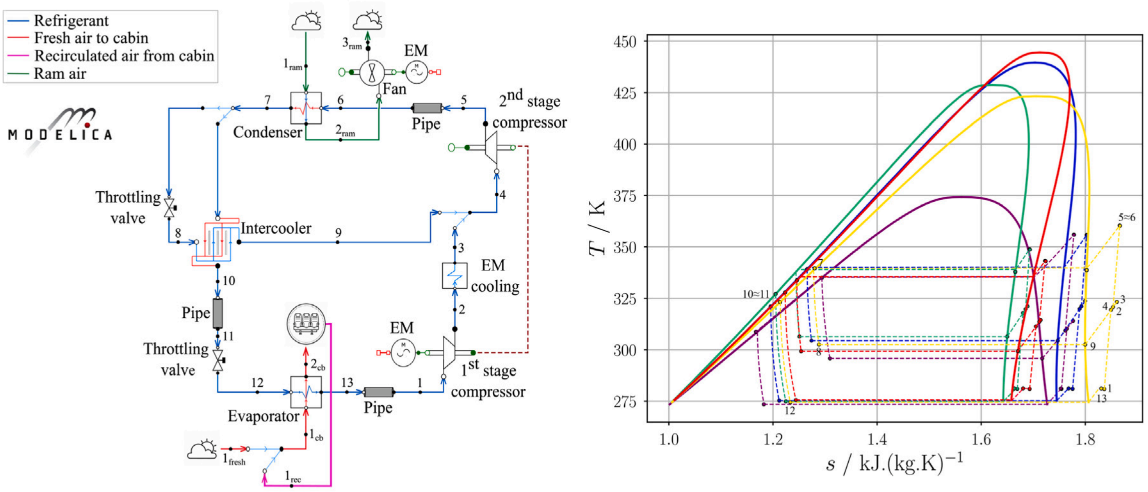

Fig. 2. Left: Graphical interface of the Modelica model of the VCC-based ECS onboard large helicopters. Right: T-s chart of the thermodynamic processes of the VCC system for each working fluid selected for the system optimization, i.e., — R-134a ($\sigma = -1.10$), — R-1233zd(E) ($\sigma = 3.92$), — R-1224yd(Z) ($\sigma = 4.91$), — R-1234ze(Z) ($\sigma = 1.50$), — R-1336mzz(Z) ($\sigma = 9.24$).

for a fixed cooling demand, the vapour quality of the refrigerant entering the evaporator decreases, thus allowing for a reduction of the refrigerant mass flow rate within the system, and enabling a reduction of the power absorbed by the compressor (Mannini, 1995). Fig. 2 shows the graphical interface of the Modelica model used for the simulation of a single VCC system pack.

Fig. 2 shows a comparison of the thermodynamic cycles on the T-s chart of the working fluids listed in Table 1. Ascione et al. (2021) demonstrated that the system COP increases if these refrigerants are used in place of R-134a. In particular, if the cooling capacity and the evaporation temperature are fixed, the following observations are valid: (i) in the case of isentropic dew-line fluids (R-1233zd(E) and R-1234ze(Z)), the large latent heat of evaporation causes a reduction of the cycle mass flow rate, with a consequent decrease of the compressor power demand; (ii) in the case of dry fluids (R-1336mzz(Z) and R-1224yd(Z)), despite the small latent heat of evaporation, the shape of the saturated liquid and vapour curves allows for a significant reduction of the losses associated with vapour superheating along the compression.

4. Models

The integrated design optimization of the system described in Section 3 has been performed, accounting simultaneously for the selection of the optimal working fluid. For modelling purposes, the in-house *DeSimECS* (Design and Simulation of Energy Conversion Systems) library has been used Ascione et al. (2024). The library is developed using the object-oriented Modelica language (Modelica Association, 2021) and features a collection of mechanical, electrical, hydraulic, and thermal component models that can be used for the steady-state simulation of a variety of energy conversion systems. The models implemented in the *DeSimECS* library can be used for both *design* and *off-design* simulations, by leveraging the acausal modelling paradigm.

Fig. 2 shows the Modelica graphical representation of the model of the helicopter ECS, resembling its simplified process flow diagram. The main components of the VCC system are the twin-stage centrifugal compressor, the evaporator, the condenser, the intercooler, and the piping. A detailed description of all the system component models can be found in the work by Ascione et al. (2024), which also treats the issues associated with the robustness of the numerical solver when simulating such a complex system. To overcome this limitation, in this study, the preliminary design model of the twin-stage centrifugal compressor is decoupled from the Modelica system model, thus the compressor design is performed using the in-house code *TurboSim*. This program is coded in Python, is tailored to the design of single-stage and twin-stage centrifugal compressors, and is validated with experimental data (Giuffré et al., 2022b,a).

4.1. Heat exchangers

The three HEXs equipping the VCC system are the evaporator, condenser, and intercooler. Both the condenser and the evaporator operate with air and two-phase refrigerant, arranged in an unmixed cross-flow configuration. These two HEXs have the same topology, i.e., a stack of alternate flat tubes with minichannels and multilouvered fins brazed together. This specific HEX geometry is typically employed for radiators in automotive applications since it is characterized by a compactness factor (β) around 1100 m^2 m^{-3}, high thermal efficiency, and low weight (Zohuri, 2017). Fig. 3 shows a schematic of the main geometrical features of this type of HEX.

The intercooler is a chevron brazed plate HEX (PHEX), whose geometry is displayed in Fig. 3. The working fluids are subcooled liquid refrigerant and two-phase refrigerant undergoing evaporation. The compactness factor usually ranges from 120 to 230 m^2 m^{-3} (Zohuri, 2017). The main modelling challenge related to these devices is accounting for the variation of refrigerant properties over the phase change which should not lead to excessive computational time. In this work, such a problem was solved by using the Moving Boundary (MB) method in place of the Finite Volume (FV) discretization method, as proposed by Bendapudi et al. (2008). This methodology consists in subdividing the HEX into a number of control volumes (CVs) equal to the number of refrigerant phases encountered along the HEX. For instance, the condenser features three CVs, namely, the desuperheating CV (superheated vapour), the condensation CV (two-phase flow), and the subcooling CV (subcooled liquid). The equations of mass and energy balance are solved for each control volume. The size of each CV is determined by the refrigerant enthalpy difference for the specific phase and the heat transfer rate. The models are steady-state and lumped parameters, hence they rely on the assumption of a linear distribution of the specific enthalpy within each CV. This allows for the calculation of the thermodynamic properties of the flow by averaging the properties at the boundaries of each CV.

Depending on the HEX type, the working fluid, and the refrigerant phase, specific heat transfer coefficient and friction factor correlations have been implemented. In the case of two-phase flow, the void fraction and the average density of the refrigerant in the control volumes

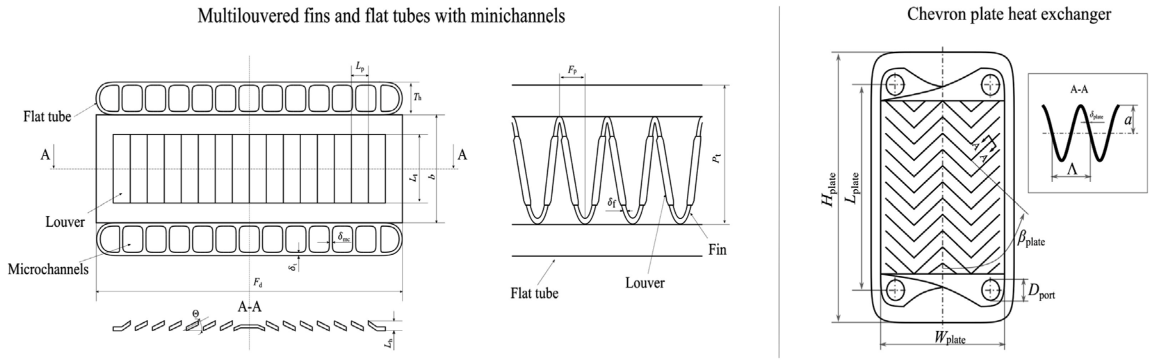

Fig. 3. Left: schematic of the HEX core geometry featuring multilouvered fins and flat tubes with minichannels. These HEX core configurations are adopted for the evaporator and the condenser. Right: schematic of the chevron plate HEX geometry used for the intercooler.
Source: Both schematics are adapted from Ascione et al. (2024).

Table 2
List of references to the correlations used for the calculation of heat transfer coefficient and pressure drop for the minichannels and multi-louvered fins HEXs, and for the chevron PHEX.

Minichannels and multi-louvered fins HEXs		
Working fluid	Property	Reference
Air	Heat transfer coefficient	Chang and Wang (1997)
Air	Pressure drop	Kim and Bullard (2002)
Refrigerant: single phase	Nusselt number	Gnielinski (2013)
Refrigerant: condensation	Heat transfer coefficient	Shah (2019)
Refrigerant: evaporation	Heat transfer coefficient	Kandlikar (1990)
Refrigerant: single phase	Pressure drop	Kast et al. (2010)
Refrigerant: two-phase flow	Pressure drop	Friedel (1979)
Chevron PHEX		
Working fluid	Property	Reference
Refrigerant: single phase	Heat transfer coefficient	Martin (1996)
Refrigerant: evaporation	Heat transfer coefficient	Cooper (1984)
Refrigerant: single phase	Pressure drop	Martin (1996)
Refrigerant: evaporation	Pressure drop	Lockhart (1949)

are estimated assuming that the homogeneous flow model holds. This assumption may lead to an underestimation of the refrigerant charge in the system (Bendapudi et al., 2008), as well as of the working fluid pressure drop across the condenser and evaporator. Table 2 lists the references to these correlations and a detailed list of the equations documented by Ascione et al. (2024). The heat transfer rate between the two flow streams is calculated using the ϵ-NTU method, while the heat transfer surface is calculated according to the methodology proposed by Shah and Sekulić (2003).

The HEXs models also include a methodology for the calculation of the dry weight of the devices, without accounting for the weight of the working fluid. The relation used for the weight estimation of the tubes and fins HEXs is described by Giuffré et al. (2023). In the case of the PHEX, due to the complexity of the chevron corrugation patterns, the volume is approximated as the number of plates times the volume of a single plate, computed without accounting for additional volume due to the corrugations. Thus, as shown by the following equations

$$\begin{cases} \text{weight}_{\text{PHEX}} = \rho_{\text{material}} V_{\text{PHEX}} \\ V_{\text{PHEX}} = \delta_{\text{plate}} H_{\text{plate}} W_{\text{plate}} N_{\text{plate}} \end{cases} \tag{2}$$

the weight is obtained by multiplying the HEX dry volume by the density of the material, which is Aluminium 3003.

The HEXs models can be used for both *design* and *off-design* simulations because of the adoption of an acausal modelling paradigm: details about the *on/off-design* methodology are documented by Ascione et al. (2024).

The condenser model has been validated through a comparison of numerical results with the findings of an experimental study conducted by Kim and Bullard (2022). The authors investigated the performance of microchannel condensers for a room air conditioning system. The validation reveals a discrepancy of less than 4% in the heat transfer surface calculation and a deviation of approximately 10% in the pressure drop estimation. A comparison in terms of heat transfer coefficient was not possible as this variable was not reported in the referenced study.

A commercial software for HEX design (Aspen Technology, 2008) has been used for the PHEX model verification. The comparison reveals a deviation of 2% in the heat transfer surface computation and less than 1% discrepancy in the outlet flow temperature calculation. The deviation in estimating the heat transfer coefficient for the single-phase and two-phase refrigerant flows is around 18% and 5%, respectively.

4.2. *Compressor*

The centrifugal compressor is electrically-driven and features two stages. A single shaft is used for both the impeller wheels, which run on gas bearings operating with the refrigerant vapour. To cope with the maximum allowable axial load of the gas bearings, the two impellers are arranged in a back-to-back configuration to balance the axial thrust (Fig. 4). To comply with the requirements of compactness, the flow at the first stage discharge section is used as coolant of the electric motor before entering the second stage. The resulting compressor assembly is thus small and does not rely on external cooling flows for thermal management. However, the drawback is that the refrigerant vapour is heated while flowing from the first to the second compressor stage, leading to a fluid dynamic efficiency penalty. For simplicity, the cooling of the bearings is disregarded in this work.

The twin-stage centrifugal compressor is modelled with the in-house tool *TurboSim*, whose development and validation are documented by Giuffré et al. (2022b,a). For the sake of conciseness, only the main steps of the compressor design methodology are recalled here.

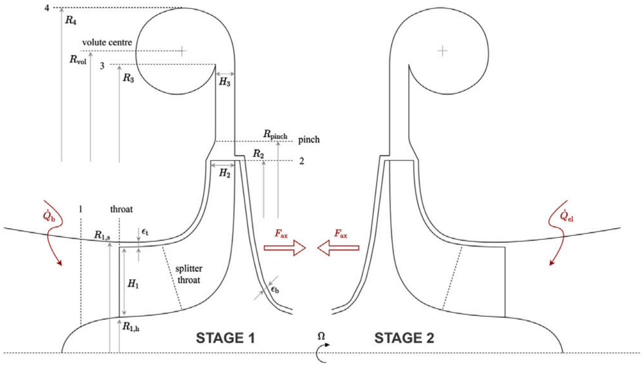

Fig. 4. Simplified schematic of the twin-stage centrifugal compressor meridional view. After (Giuffré et al., 2022a).

Fig. 4 illustrates a simplified schematic of the twin-stage centrifugal compressor assembly. The design of each stage of the centrifugal compressor depends on the choice of eight non-dimensional design variables, namely, the swallowing capacity

$$\phi_{t1} = \frac{\dot{m}}{\rho_{t1} U_2 D_2^2}, \tag{3}$$

the isentropic loading coefficient

$$\psi_{is} = \frac{\Delta h_{tt,is}}{U_2^2}, \tag{4}$$

the impeller shape factor

$$k = 1 - \left(\frac{R_{1,h}}{R_{1,s}}\right)^2, \tag{5}$$

the impeller outlet absolute flow angle α_2, the number of blades N_{bl}, the diffuser radius ratio R_3/R_2, and two non-dimensional parameters $R_{r,pinch}$ and $H_{r,pinch}$ which define the diffuser shape. Moreover, the design process requires some specifications, such as the nominal total-to-total pressure ratio β_{tt}, the nominal refrigerant mass flow rate $\dot{m}$, the working fluid, the nominal total inlet conditions, and geometric parameters imposed by manufacturing limitations, e.g., the impeller tip clearance gap. In this work, a constant value of 0.5 is assigned to both $R_{r,pinch}$ and $H_{r,pinch}$, whereas the impeller tip clearance and the back-face clearance are set to 0.15 mm.

The impeller wheels of the twin-stage compressor are installed on the same shaft. This means that the rotational speed of the second stage is dependent on the design parameters chosen for the first stage design. In particular, for an assigned isentropic loading coefficient of the first stage, that of the second stage is defined accordingly.

The compressor design method relies on the lumped parameters approach. With reference to Fig. 4, the flow properties are calculated at four locations for each compressor stage. These are inducer inlet, impeller outlet, diffuser outlet, volute outlet. Moreover, a more refined discretization method is adopted at some prescribed locations to better capture the variation of the flow properties. In particular, the flow at the inducer inlet is evaluated at five different span-wise locations, while the flow throughout the vaneless diffuser is discretized over 100 computational nodes (Giuffré et al., 2022b,a). The fluid-dynamic losses within the turbomachinery are predicted through semi-empirical correlations, as reported by Giuffré et al. (2022b). Downstream of the impeller, the compressor is equipped with a vaneless diffuser, where the flow is modelled resorting to the two-dimensional system of equations proposed by Stanitz (1952). The axial thrust acting on gas bearings is estimated following the method introduced by Tiainen et al. (2021). The research documented in this work concerns the preliminary design of the centrifugal compressor, however, the compressor model also allows for off-design simulations to retrieve the operating map of the turbomachinery.

The compressor model has been validated by comparing the results of the in-house tool with the experimental data of three test cases available in the open literature (Eckardt, 1975, 1976, 1977; Japikse, 1987; Schiffmann and Favrat, 2009, 2010), and with the outcome of the CFD simulation of a new compressor prototype (Giuffré et al., 2022a). As a result, more than 95% of the experimental and CFD data fall within the ± 5% uncertainty bands of the in-house tools predictions.

The compressor model is complemented with a method for preliminary weight estimation. The weight of the compressor assembly is computed by resorting to CadQuery (Urbańczyk et al., 2020), i.e., an open-source Python library for parametric 3D CAD modelling. Once the dimensions of the main components are set, a simplified CAD model of the compressor assembly is automatically generated. Next, the weight of each component is computed according to its volume and the prescribed material. In this work, following the indication of the industrial partners, the material selected for the compressor is the 2219-T852 aluminium alloy. Moreover, the weight of the electric motor is estimated based on the trends of power density for high-speed permanent magnet synchronous machines documented by Van Der Geest et al. (2015). The correlations implemented in the compressor model are derived by assuming optimal forced air cooling to keep the magnet temperature below the threshold of 150 °C and are valid for rotor surface speeds up to 200 $\mathrm{m\ s^{-1}}$ and electrical powers as high as 1 MW. The final weight of the entire compressor assembly also includes the Electronic Control Unit (ECU), whose weight is assumed as fixed and equal to 7.5 kg, based on information provided by the industrial partners.

5. Methodology

The objective of this work is the investigation of the effects of adopting new low-GWP refrigerants on the optimal design of a VCC system for helicopter ECS. This goal is achieved by using a novel methodology that allows for the integrated design optimization of the system, i.e., the thermodynamic cycle performance and system components design are optimized simultaneously. An in-house software was developed for such purpose and tested on a case in which the working fluid was R-134a, as documented in Ascione et al. (2024).

5.1. Multi-objective integrated system design optimization

The multi-objective optimization (MOO) problem is the same as the one described by Ascione et al. (2024), where the objective functions $f_q(x)$ are the COP and the system weight. In particular, the weight is computed as the sum of that of the three HEXs, the piping, and the centrifugal compressor. Given a set of design variables x_n and inequality constraints $g_j(x)$, the optimization problem is mathematically expressed as

$$\begin{aligned} &\min/\max \quad f_q(x), \quad q = 1,\dots,Q \quad \forall x \in \mathbb{R}, \\ &\text{s.t.} \quad \begin{cases} g_j(x) \le 0, & j = 1,\dots,J \\ x_n^{(L)} \le x_n \le x_n^{(U)}, & n = 1,\dots,N. \end{cases} \end{aligned} \tag{6}$$

A Genetic Algorithm (GA) has been chosen to determine the non-dominated solutions populating the Pareto front. Fig. 5 illustrates the logic of the integrated system optimization framework.

When the simulation starts, the optimization algorithm assigns to each individual **N** of a generation, a vector of **M** design variables $\mathbf{X_{NxM}}$. Each vector groups the variables related to the HEXs ($\mathbf{X_{HEXs}}$) and the centrifugal compressor ($\mathbf{X_C}$) design

$$\mathbf{X_{NxM}} = [\mathbf{X_{HEXs}}, \mathbf{X_C}]. \tag{7}$$

For each vector of design variables, the software executes a routine for the preliminary calculation of the reduced inlet thermodynamic properties of both compressor stages and the refrigerant mass flow rate

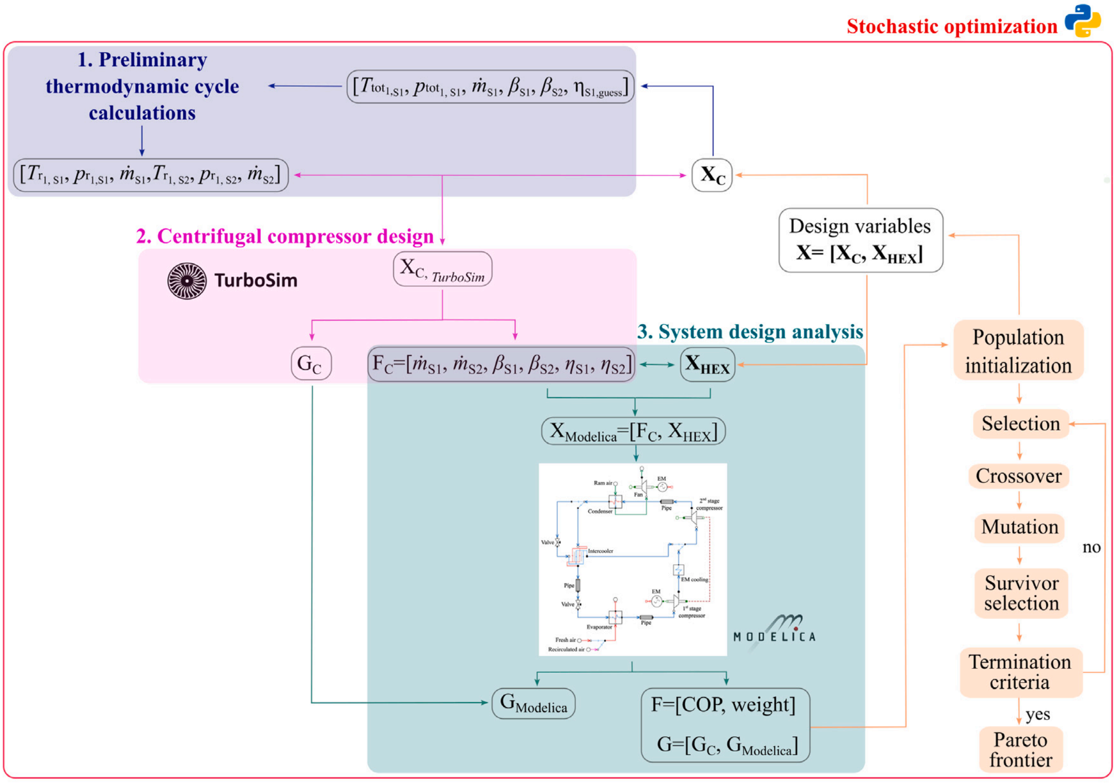

Fig. 5. Flowchart illustrating the methodology implemented for the integrated design optimization of the helicopter ECS.

of the second stage. These values, together with the set of variables $\mathbf{X}_\mathbf{C}$, are given as input to *TurboSim*. Once, the compressor design is finalized, the values of total-to-total efficiency, compression ratio, and refrigerant mass flow rate of both stages are added to the vector of design variables $\mathbf{X}_{\mathbf{HEXs}}$. This new group of design variables includes all the input data necessary to simulate the Modelica model of the VCC system. Note that the VCC system compressor model is considerably simplified with respect to that implemented in *TurboSim* (Giuffré et al., 2022a), having the efficiency and the compression ratio as the only input parameters. Once initialized, the GA algorithm continues with the processes of selection, crossover, and mutation. This routine is iterated until the termination criteria are reached and the Pareto front of optimal solutions is obtained.

5.2. Case study

The integrated design optimization framework described in Section 5.1 has been tested on the design of a VCC system for a large rotorcraft ECS hosting 20 passengers and 2 pilots. The case study focuses on the design of the rotorcraft ECS, with the design point representing a critical operating condition: the helicopter is on the ground on a hot and humid day (ARP292, 2014). The ambient temperature is 40 °C and the relative humidity is 40%. Table 3 lists the operating parameters chosen for the system simulation. Furthermore, the complete list of parameters selected for the design of the system HEXs can be found in the Appendix (Table 10).

The optimization problem consists of 24 design variables (Table 4) whose range of variation is set the same for all the considered working fluids, and 26 inequality constraints (Table 5). The stochastic optimization algorithm chosen for this application is the Non-Sorted Genetic Algorithm II (NSGA-II) available in the open-source Python library Pymoo (Blank and Deb, 2020). Each population comprises 220 individuals, namely 10 individuals for each design variable. For the initial points sampling, a random approach has been chosen for integer variables, and the Latine hypercube method is used in the case of real variables. The thermodynamic and transport properties of the working fluids have been computed through a well-assessed commercial database (Lemmon et al., 2018).

Table 3
Operating parameters for the ECS in the case of helicopter on the ground on a hot and humid day. The design point is equivalent to the one considered by Ascione et al. (2024).

Rotorcraft ECS for cabin air conditioning		
Refrigerant loop		
Evaporation temperature	$T_{eva}/°C$	0
Evaporator cooling duty	$\dot{Q}_{eva}/kW$	12.5
Air side		
Environmental air temperature	$T_{air,env}/°C$	40
Recirculated cabin air temperature	$T_{air,rec}/°C$	28
Ram air mass flow rate	$\dot{m}_{ram}/kg\ s^{-1}$	1.1
Fresh cabin air mass flow rate	$\dot{m}_{fresh,cb}/kg\ s^{-1}$	0.1
Recirculated cabin air mass flow rate	$\dot{m}_{rec,cb}/kg\ s^{-1}$	0.5

A unique Modelica system model is used to test all the different refrigerants, hence, any difference in the computational time needed to reach convergence is only dependent on the complexity of the equation of state model. On average, 7 days of computational time is needed to reach convergence on a standard desktop workstation with a CPU Intel(R) Xeon(R) CPU E5-1620 v3 featuring 8 logical cores.

6. Results and discussion

A Pareto front of optimal solutions is obtained for each working fluid, aside from R-1336mzz(Z) (Fig. 6) because if this is the working fluid the algorithm could not determine any non-dominated solution due to the violation of some of the constraints related to the centrifugal compressor design, as discussed in Section 6.2. Fig. 6 shows that, compared to R-134a, low-GWP refrigerants always allow for more efficient and lighter system designs. In particular, R-1234ze(Z) can be deemed as

Table 4
Design variables selected for the design optimization problem.

Design variables			
Variable	Symbol	Min. value	Max. value
Louver angle (evap. and cond.)	$\Theta/^\circ$	25	35
Louver pitch (evap. and cond.)	L_p/mm	0.50	3
Louver length (evap. and cond.)	L_l/mm	2.13	18.5
Evaporator height	$H_\mathrm{eva}/\mathrm{mm}$	100	700
Condenser height	$H_\mathrm{cond}/\mathrm{mm}$	100	500
HEX depth (evap. and cond.)	$D_\mathrm{HEX}/\mathrm{mm}$	20	60
Compression ratio (1st, 2nd stage)	$\beta_\mathrm{tt}/-$	2	4
Swallowing capacity (1st, 2nd stage)	$\Phi_\mathrm{t1}/-$	0.02	0.20
Shape factor (1st, 2nd stage)	$k/-$	0.65	0.95
Absolute outlet angle (1st, 2nd stage)	$\alpha_2/^\circ$	60	75
Number of blades (1st, 2nd stage)	$N_\mathrm{bl}/-$	10	20
Diffuser to outlet impeller radius ratio (1st, 2nd stage)	$R_3/R_2/-$	1.2	2
Loading coefficient (2nd stage)	$\Psi/-$	0.65	1
Refrigerant mass flow rate (1st stage)	$\dot{m}_\mathrm{refr}/\mathrm{kg\ s^{-1}}$	0.05	0.15

Table 5
Inequality constraints selected for the design optimization problem.

Constraints values			
Variable	Symbol	Min. value	Max. value
HEX width (evap. and cond.)	$W_\mathrm{HEX}/\mathrm{mm}$	50	800
Refrigerant velocity (evap. and cond.)	$v_\mathrm{refr}/\mathrm{m\ s^{-1}}$	–	20
Air velocity (evap. and cond.)	$v_\mathrm{air}/\mathrm{m\ s^{-1}}$	–	20
ΔT at pinch point (condenser)	$\Delta T_\mathrm{pp,cond}/\mathrm{K}$	5	20
Refrigerant pressure drop (evap. and cond.)	$\Delta p_\mathrm{refr}/\mathrm{bar}$	–	0.8
Air pressure drop (evap. and cond.)	$\Delta p_\mathrm{air}/\mathrm{Pa}$	–	400
Inlet hub radius (1st, 2nd stage)	$R_\mathrm{1,hub}/\mathrm{mm}$	2.35	–
Outlet blade height (1st, 2nd stage)	$H_\mathrm{2,blade}/\mathrm{mm}$	0.6	–
Outlet relative blade angle (1st, 2nd stage)	$\beta_\mathrm{2,blade}/^\circ$	−45	−10
Rotational speed (1st, 2nd stage)	Ω/krpm	10	200
Inlet relative Mach at shroud (1st, 2nd stage)	$M_{w_{1,s}}/-$	–	1.4
Outlet relative Mach at shroud (1st, 2nd stage)	$M_{w_{2,s}}/-$	–	0.98
Absolute Mach at diffuser outlet (1st, 2nd stage)	$M_3/-$	–	0.70
Net axial thrust twin-stage compr.	$F_\mathrm{axial}/\mathrm{N}$	0	26

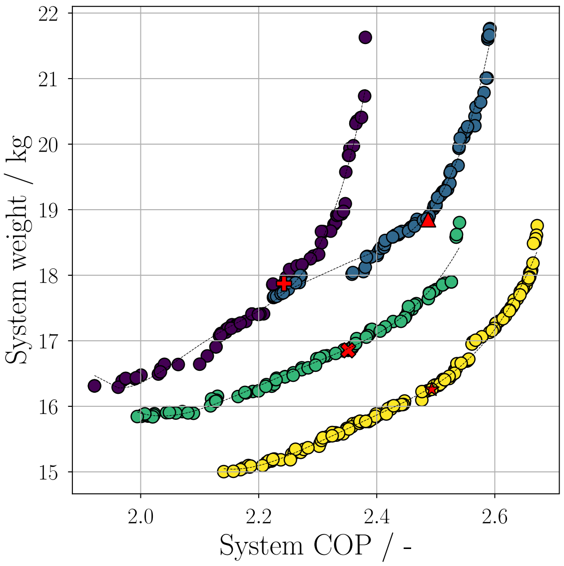

Fig. 6. Pareto fronts associated with the considered working fluids resulting from the system optimization in terms of system weight and COP. The working fluids are (●) R-134a, (●) R-1233zd(E), (●) R-1224yd(Z), (●) R-1234ze(Z). Optimal system design points selected according to the approach discussed in Section 6.3 (✚, ▲, ✖, ★).

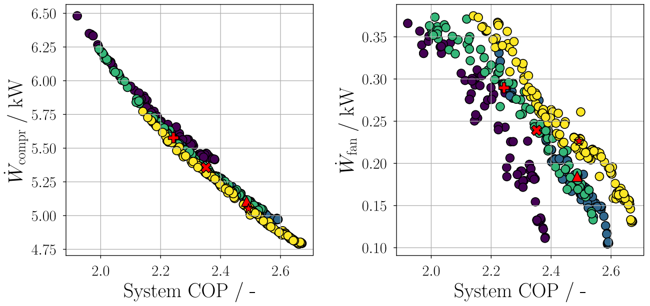

Fig. 7. From left to right: centrifugal compressor and ram air fan electric power demand as a function of the system COP. Working fluids: (●) R-134a, (●) R-1233zd(E), (●) R-1234ze(Z), (●) R-1224yd(Z).

the best working fluid, enabling a 12% increase in efficiency and a 26% reduction in weight. Despite the enhancement in terms of COP with respect to R-134a, the use of R-1233zd(E) is always associated with the design of heavier system components if compared to the other two HFOs. Finally, if R-1224yd(Z) is the working fluid, the system exhibits a performance that is a compromise between that of R-1233zd(E) and R-1234ze(Z).

In this work, the COP has been defined as the ratio between the evaporator cooling capacity and the total electric power needed to drive all the turbomachinery installed in the system, i.e., the fan and the centrifugal compressor

$$\mathrm{COP} = \frac{\dot{Q}_\mathrm{eva}}{\dot{W}_\mathrm{compr} + \dot{W}_\mathrm{fan}}. \tag{8}$$

As expected, the electric power demand decreases as a function of the system efficiency (Fig. 7). In particular, the power needed to drive the fan varies in a range from 0.10 kW to 0.38 kW, depending on the pressure drop in the ram air stream delivered to the condenser. The root cause of the difference in terms of system COP between the working

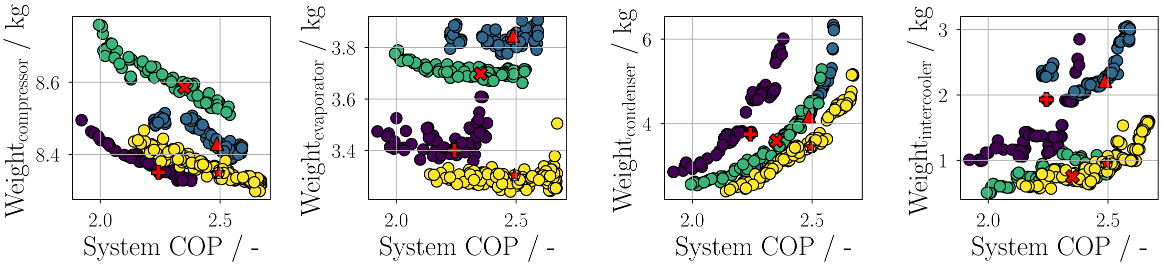

Fig. 8. Trend of the weight of the main system components as a function of the system COP. Working fluids: (●) R-134a, (●) R-1233zd(E), (●) R-1234ze(Z), (●) R-1224yd(Z). From left to right: centrifugal compressor, evaporator, condenser, and intercooler.

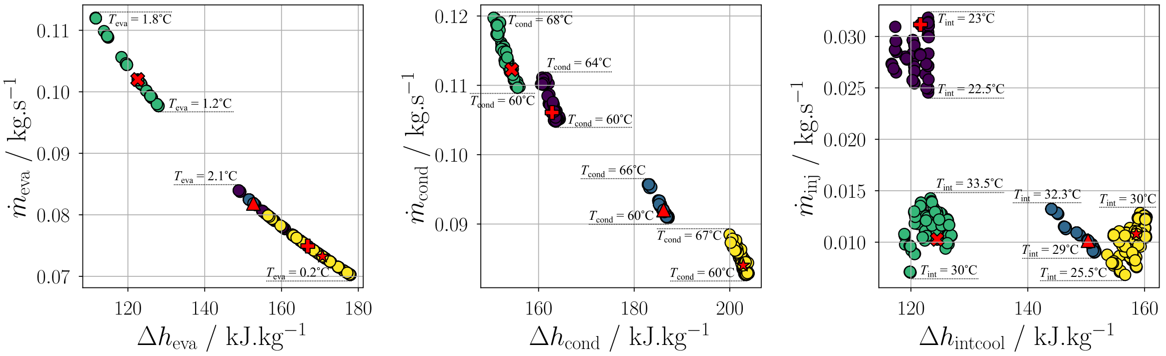

Fig. 9. Refrigerant mass flow rate as a function of the specific enthalpy variation for each heat exchanger, and corresponding range of operating temperature. From left to right: evaporator, intercooler and condenser. Working fluids: (●) R-134a, (●) R-1233zd(E), (●) R-1234ze(Z), (●) R-1224yd(Z).

fluids is the centrifugal compressor power demand, which ranges from 4.5 kW to 6.5 kW.

Fig. 8 displays the breakdown of the total system weight into those of the main system components as a function of the COP and the prescribed refrigerant. The piping weight is included in the overall calculation, but it is not shown in Fig. 8 since its value is negligible with respect to those of the HEXs and the compressor. The heaviest system component is the compressor. Its weight ranges from 8.3 kg to 8.8 kg and it decreases for more efficient system designs, since the compressor power demand is reduced. According to the methodology described in Section 4.2, the weight of the ECU is independent of the working fluid and equal to 7.5 kg, therefore the differences observed among the working fluids are only associated with the sizing of the compressor wheel, the casing, and the electric motor. The compressor weight calculation depends on parameters, e.g. wall thickness, and back face disc thickness, which are meant to be selected only for detail design. Therefore, the values of weight reported in this manuscript are approximate and they are only meant to indicatively show the dependence between working fluid and compressor weight, which is not expected to exceed a maximum of 2.5 kg given the small values of electric power demand. The results confirm that the use of the HFOs leads to the design of a larger compressor with respect to R-134a. Among the HFOs, R-1234ze(Z) would lead to the heaviest optimal compressor designs. Even if its vapour density is similar to that of R-1224yd(Z), a larger amount of refrigerant mass flow rate is needed in the VCC loop because of the small specific enthalpy difference across the evaporator (Fig. 9). Thus, larger flow passages are required within the compressor.

Among the HEXs, the condenser is the heaviest component and its weight variation as a function of the system COP is the widest among all the system components (Fig. 8). The condenser weight is almost independent of the choice of the working fluid since its sizing is a consequence of the ram air pressure drop, thus the electric fan power consumption minimization. Hence, heavier condensers, featuring large ram air frontal areas, are necessary for high-efficiency systems.

Contrarily, the evaporator weight is independent of the COP, but it is strongly influenced by the choice of the working fluid. The heaviest devices are designed in the case of R-1233zd(E). Among the selected HFOs, this refrigerant is characterized by the lowest density, implying the need for larger flow passages to limit the velocity of the refrigerant, hence the associated pressure drops. Note that, for a prescribed cooling capacity in the evaporator, the specific enthalpy variation of R-1233zd(E) is similar to the one of R-134a (Fig. 9). Therefore, the refrigerant mass flow rate is comparable, and any difference in the HEX weight can only be associated with the effect of the fluid density. In the case of R-1224yd(Z), despite the similarities in terms of thermodynamic properties with R-1234ze(Z), the evaporator weight is different. Fig. 9 shows that the mass flow rate of R-1224yd(Z) within the evaporator is larger as compared with that calculated for the other refrigerants. This aspect, combined with the effect of the flow density, makes the size of this HEX similar to the one for the R-1233zd(E) system. In the case of R-1234ze(Z), the optimal designs correspond to evaporators whose weights are closer to those for R-134a. This is explained considering that, despite the large difference in terms of flow density, the mass flow rate of this refrigerant is the lowest if compared to those computed for the other haloolefins, thanks to the large latent heat of evaporation. This effect compensates for the effect associated with the low flow density, leading to compact evaporators.

Finally, the results show that the sizing of the intercooler is similar for all the working fluids. Its weight oscillates between 0.5 kg and 3 kg. The only variable influencing the intercooler sizing, hence its weight, is the plate length (L_{plate}). The heat duty of this HEX ranges from 1 kW to 2 kW in the case of the haloolefins, and it increases from 3 kW to 4 kW for R-134a. The heaviest component is sized for the case of R-1233zd(E). Despite the similar values of the mass flow rate of R-1224yd(Z) and R-1234ze(Z) (Fig. 9), the lower refrigerant density of R-1233zd(E) implies larger flow passages, therefore a bulkier and heavier component (Fig. 8).

6.1. Heat exchangers design

According to the adopted design requirements, the cooling capacity of the evaporator is specified and equal to 12.5 kW. From Eq. (8), the

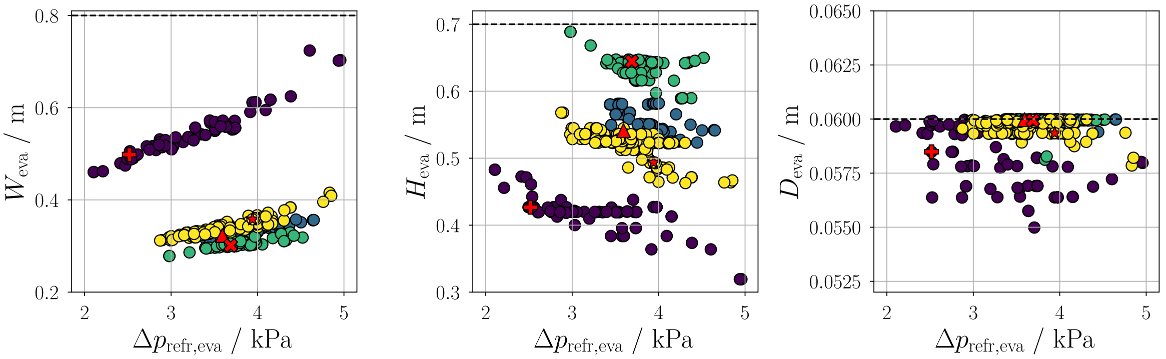

Fig. 10. Trend of the three dimensions of the evaporator core (from left to right: width, height, and depth) as a function of pressure drop associated with the refrigerant flow. Working fluids: (●) R-134a, (●) R-1233zd(E), (●) R-1234ze(Z), (●) R-1224yd(Z).

Table 6
Values defining the optimal fins geometry and the aerothermal performance of the evaporator. These values are calculated as an average of those related to optimal designs for each refrigerant.

Variable	Symbol	R-134a	R-1233zd(E)	R-1224yd(Z)	R-1234ze(Z)
Louver angle	$\Theta/°$	34.5	34.1	34.7	33.8
Louver length	L_{l}/mm	10.6	5.90	7.10	7.40
Louver pitch	L_{p}/mm	0.50	0.50	0.50	0.50
Refrigerant flow velocity	v_{refr}/m s^{-1}	2.5	5.7	5.8	5.4
Refrigerant heat transfer coefficient	h_{refr}/kW m^{-2} K^{-1}	1.97	6.07	5.05	5.13
Air flow velocity	v_{air}/m s^{-1}	2.3	2.8	2.7	2.9
Air heat transfer coefficient	h_{air}/W m^{-2} K^{-1}	121	133	142	128
Air pressure drop	Δp_{air}/Pa	173	218	208	230

only variable which affects the evaporator sizing in case the system COP is to be maximized is the pressure drop associated with the refrigerant flow. Fig. 10 illustrates the trend of the three dimensions of the evaporator core as a function of the refrigerant pressure drop.

The optimal evaporator designs are characterized by a short width and a large height. These designs feature a large number of short tubes to decrease the refrigerant velocity and shorten the flow path. The optimal depth of the evaporator is the same for all the fluids, and its value corresponds to the upper bound of the range selected for this design variable (see Table 5). Notice that the value of H_{eva} is larger in the case of haloolefins, because of the larger frontal area needed to reduce the flow speed in the case of low-density refrigerants and obtain a pressure drop in the same range as that calculated for R-134a. Table 6 lists the values of the fin geometrical parameters and of the variables related to the aerothermal performance of the evaporator, calculated as an average of the values related to the optimal designs. In the case of low-GWP refrigerants, the flow velocity is almost double that of R-134a, with a consequent similar trend for the heat transfer coefficient. Such high values allow the design of compact-size evaporators despite the limitations associated with the fluid density when operating at low-pressure levels. Finally, the size of the fins is similar, independently from the working fluid. The same is valid for the performance of the ram air side, as reported in Table 6.

As opposed to the design of the evaporator, the condenser sizing is driven by the need to minimize the fan power demand, hence the ram air pressure drop. As reported by Ascione et al. (2021), in the case of ground operating conditions, the necessary ram air mass flow rate is approximately equivalent to $1.1\ \mathrm{kg\ s^{-1}}$, see the design specifications listed in Table 3. Hence, to enhance the system efficiency while minimizing friction losses, the condenser must feature a large ram air frontal area (Fig. 11). Fig. 7 shows that the electric fan power demand and the air pressure drop are almost independent from the selected working fluid. Therefore, the minimum ram air pressure drop is achieved in correspondence with the largest value of condenser width, see Table 5. Finally, the optimal condenser depth does not depend on the adopted working fluid and corresponds to the minimum value that this variable can assume within the prescribed design space (Fig. 11).

Table 7
Optimal condenser fin design parameters. These values are calculated as an average of the optimal design points over the Pareto front of each refrigerant.

Variable	Symbol	R-134a	R-1233zd(E)	R-1224yd(Z)	R-1234ze(Z)
Louver angle	$\Theta/°$	29.2	28.5	28.8	29.5
Louver length	L_{l}/mm	9.5	10.6	10.7	9.2
Louver pitch	L_{p}/mm	1.9	2.6	2.6	2.9

Table 7 summarizes the fin geometry of the condenser for all the refrigerants. The fin geometry is very similar for all the fluids, except for the louver pitch, whose largest values are calculated in the case of haloolefins. This can be justified considering that larger flow pitches allow for lower pressure drops to guarantee an optimal trade-off between friction loss reduction and HEX compactness on the ram air side.

As discussed thus far, for a constant ram air mass flow rate, the optimal condenser dimensions are independent of the working fluid selection, and the same is valid for the airflow velocity. Consequently, the range of variation of the heat transfer coefficient is similar for all refrigerants on both sides of the condenser, as shown in Fig. 12. Finally, for what regards the refrigerant side, the effect of flow density has a strong influence on the condenser sizing. Since the global size of the HEX, the condensation temperature, and the refrigerant mass flow rate (see Fig. 9) are comparable for all the working fluids, condensers designed for haloolefins are always characterized by higher flow velocities if compared to those designed for R-134a. As a consequence, larger pressure drops occur on the refrigerant side, while the heat transfer coefficient varies in the same range of values as those calculated in case R-134a is the working fluid.

6.2. Compressor design

Table 8 lists the average value of the design variables used for the centrifugal compressor design. These values are calculated as an average of the optimal design points over the values of the Pareto front obtained for each refrigerant. The loading coefficient is similar

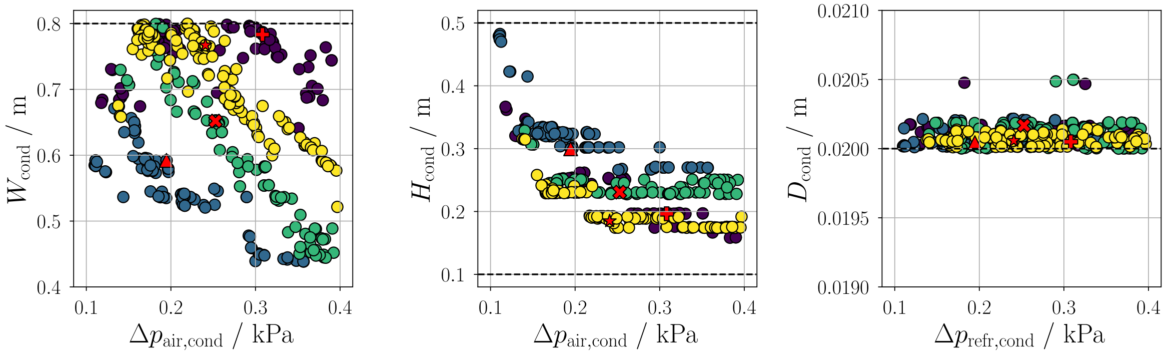

Fig. 11. Trend of the three dimensions of the condenser core (from left to right: width, height and depth) as a function of pressure drop associated with the ram air flow. Working fluids: (●) R-134a, (●) R-1233zd(E), (●) R-1234ze(Z), (●) R-1224yd(Z).

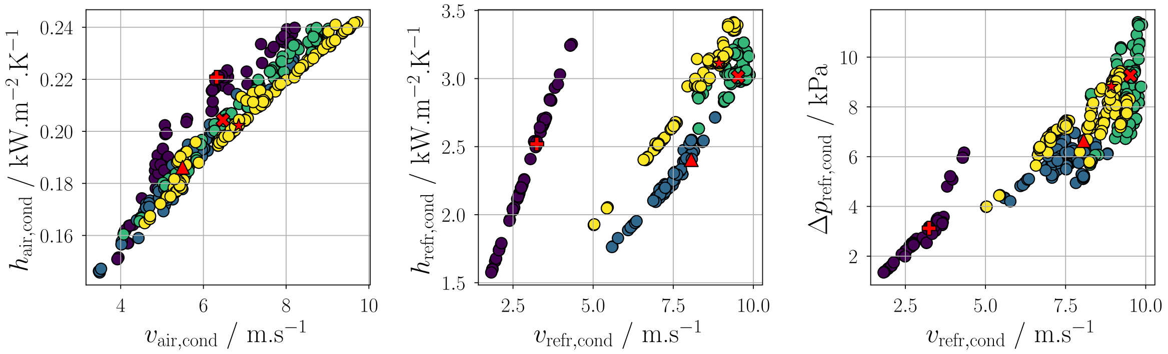

Fig. 12. Condenser aerothermal performance. From left to right: ram air heat transfer coefficient as a function of the air velocity. Refrigerant stream heat transfer coefficient as a function of the refrigerant velocity inside the condenser tubes. Pressure drop associated with the refrigerant stream as a function of the refrigerant speed within the condenser tubes. Working fluids: (●) R-134a, (●) R-1233zd(E), (●) R-1234ze(Z), (●) R-1224yd(Z).

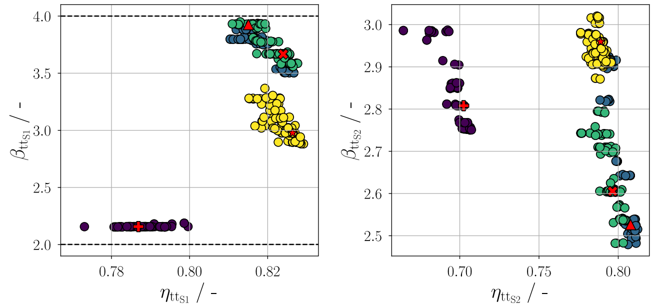

Fig. 13. Total-to-total compression ratio as a function of the isentropic efficiency of the first stage (left) and the second stage (right) of the centrifugal compressor. Working fluids: (●) R-134a, (●) R-1233zd(E), (●) R-1234ze(Z), (●) R-1224yd(Z).

for each compressor stage and does not vary significantly with the working fluid. The values of the flow coefficient and the shape factor are higher for the first stage than the second stage, and this is true also for the pressure ratio and the isentropic efficiency (Fig. 13). The reason is that there is an optimal trade-off between the interstage pressure, and thus the split of the compressor duty among the two stages, which maximizes the system efficiency and the need to satisfy the constraint on the maximum net axial thrust. The design of the second stage is technologically more challenging due to the lower volumetric flow rate associated with the higher density of the fluid. Hence, the optimal twin-stage compressor design features an unequal split of the total-to-total pressure ratio, which is lower for the second stage, in order to limit the inherent efficiency penalty. These considerations are valid for all fluids, except for the case of R-134a, and agree with the findings reported by Giuffré et al. (2022a).

In the case of R-134a, the optimal designs are characterized by higher pressure ratios of the second stage as compared to the values of the first stage (Fig. 13). This is due to the higher influence of the prescribed set of constraints on the design of such compressor. The higher density of R-134a with respect to that of the other refrigerants leads to the design of a compressor featuring a higher rotational speed, smaller dimensions, and a higher net axial thrust. The consequence thereof is a sizeable limitation of the feasible design space and ultimately the choice of very low values of the flow coefficient for both stages. Notice that the selection of a low flow coefficient for the second stage is believed to strongly penalize the operating range of the machine, thus generally leading to a sub-optimal design (Giuffré et al., 2022a). However, the maximization of the compressor operating range is not included in the set of design optimization variables, thus leading to optimal designs for R-134a featuring a higher pressure ratio and a low flow coefficient in the second stage.

Fig. 14 shows the trend of the impeller hub radius as a function of the rotational speed and of the blade height at the impeller outlet with respect to the volumetric flow rate. As compared to R-134a, haloolefins allow for larger impeller wheels for both compressor stages, as a result of the larger volumetric flow rate, thus overcoming all the challenges associated with manufacturability. Large compressor wheels inherently lead to a reduction of the rotational speed (Fig. 15). To comply with the limit on the maximum axial thrust, the rotational speed in the case of R-134a is comparable with that associated with R-1234ze(Z). Therefore, the compressors designed for these two refrigerants have similar ranges of impeller size (Fig. 14). Fig. 15 shows the trend of the net axial thrust of the twin-stage centrifugal compressor as a function of the rotation speed. For the considered design case, a maximum admissible value of the axial force equal to 26 N has been selected. The results show that the optimal compressor designs obtained for the haloolefins have a large margin of safety with respect to this limit.

Table 8
Optimal design variables for the twin-stage centrifugal compressor design. These values are calculated as an average of the optimal design points over the Pareto front associated with each refrigerant.

Variable	Symbol	R-134a		R-1233zd(E)		R-1224yd(Z)		R-1234ze(Z)	
		Stage 1	Stage 2	Stage 1	Stage 2	Stage 1	Stage 2	Stage 1	Stage 2
Swallowing capacity	$\Phi_{t1}/-$	0.07	0.03	0.15	0.07	0.12	0.06	0.16	0.07
Loading coefficient	$\Psi/-$	0.65	0.72	0.70	0.70	0.68	0.68	0.65	0.71
Shape factor	$k/-$	0.82	0.75	0.94	0.84	0.90	0.85	0.92	0.84
Outlet absolute flow angle	$\alpha_2/°$	68	73	69	70	69	71	67	71
Diffuser to outlet impeller radii ratio	$R_3/R_2/-$	1.45	1.35	1.50	1.35	1.47	1.42	1.80	1.40

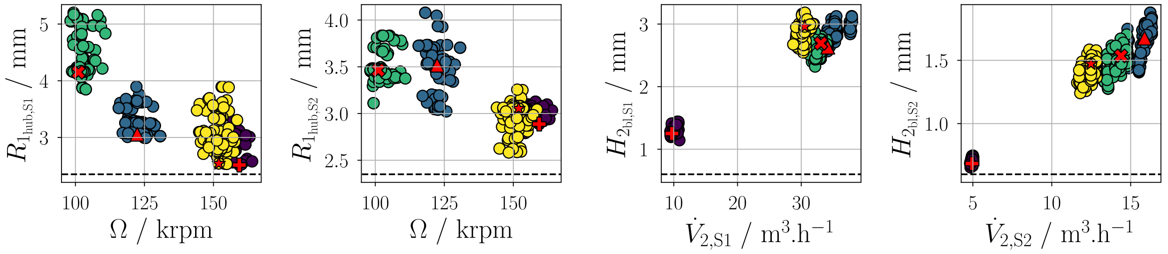

Fig. 14. Twin-stage centrifugal compressor impeller sizing. From left to right: trend of the impeller inlet radius at the hub as a function of the compressor rotational speed for both the first and the second stages. Outlet blade height as a function of the volumetric flow rate of both the first and second compressor stages. Working fluids: (●) R-134a, (●) R-1233zd(E), (●) R-1234ze(Z), (●) R-1224yd(Z).

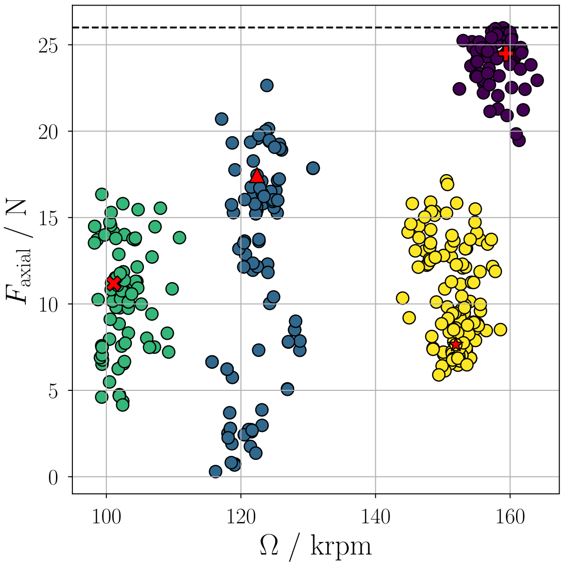

Fig. 15. Trend of the net axial thrust as a function of the rotational speed of the twin-stage centrifugal compressor and the working fluid ((●) R-134a, (●) R-1233zd(E), (●) R-1234ze(Z), (●) R-1224yd(Z)).

As mentioned in Section 6, the VCC system design optimization has also been performed in case refrigerant R-1336mzz(Z) is the working fluid. However, the optimization algorithm could not converge to any set of non-dominated solutions because of the violation of the non-linear constraint associated with the maximum admissible value of inlet relative Mach number at the impeller shroud ($M_{\text{w}_{1,\text{s}}}$), as reported in Table 5. With reference to the properties listed in Table 1, R-1336mzz(Z) is a promising alternative to R-134a: this refrigerant is not flammable or toxic, and it features the lowest value of vapour density and the highest molecular complexity among all the considered working fluids. However, higher molecular complexity implies large Mach number values of the flow through the compressor channels, as discussed in Section 2. Designs for which $M_{\text{w}_{1,\text{s}}}$ exceeds 1.4 are discarded to limit the losses associated with secondary flow and mixing due to shock interaction within the rotor flow channels, as discussed by Rusch and Casey (2013). However, to investigate whether any R-1336mzz(Z) compressor design was feasible, the constraint on the maximum inlet Mach number at the impeller shroud has been relaxed and its value set to 1.6. In this case, the system optimization converged to a limited set of non-dominated solutions. However, the optimal compressor designs feature values of design mass flow rates which are very close to those at the chocking point. Thus, despite the attractive properties of R-1336mzz(Z), the results of the system optimization reveal that the design of a twin-stage centrifugal compressor is unfeasible. Feasible compressor designs might be obtained with more than two stages.

6.3. Optimal system designs

For each working fluid, a single optimal design has been selected among those forming the Pareto front resulting from the solution of the MOO procedure (Fig. 6). It is common practice in aerospace engineering to identify the optimal system design solution as the one enabling the minimum aircraft specific fuel consumption. This quantity is defined as a linear combination of the penalties associated with system weight, power off-take and ram air drag. However, in the case of the helicopter operating on the ground, the ram air drag penalty cannot be accounted for as an objective function. Therefore, a multi-criteria decision-making algorithm based on the Augmented Scalarization Function (ASF) decomposition method has been selected (Wierzbicki, 1982). A decomposition method requires the definition of a vector of weights with a number of elements equal to the number of objective functions and formed by positive float numbers, whose sum is unitary. Such a vector defines how predominant is each one of the objectives with respect to the others for the selection of a single optimal design point out of all the non-dominated solutions forming the Pareto front. The decomposition transforms the MOO procedure into a set of single-objective optimization problems. However, since the individual objective functions usually feature different scales of values, normalization is always needed, thus

$$\bar{f}_q(x) = \frac{f_q(x) - c}{\hat{z}_q^{\text{N}} - \hat{z}_q^*}, \quad \forall q = 1, \dots, Q \tag{9}$$

where $\hat{z}_q^*$ and $\hat{z}_q^{\text{N}}$ are respectively the ideal point and the nadir point. They are known as boundary points since they define the range of the solutions to the optimization problem. In particular, the ideal point corresponds to the best of each objective function in the design space

$$\hat{z}_q^* = \min\{f_q(x) \mid x \in \Omega\}. \tag{10}$$

Table 9
List of the main system design parameters corresponding to the optimal design points chosen from the Pareto front associated with each working fluid.

Variable	Symbol	(✚) R-134a		(▲) R-1233zd(E)		(✖) R-1224yd(Z)		(★) R-1234ze(Z)	
System efficiency	COP/–	2.20		2.50		2.30		2.50	
System weight	weight/kg	17.9		18.9		16.9		16.2	
Evaporation temperature[a]	$T_{\mathrm{eva}}/°\mathrm{C}$	0.2		1.6		1.5		1.3	
Intermediate temperature	$T_{\mathrm{int}}/°\mathrm{C}$	22.6		32.3		31.3		26.5	
Condensation temperature	$T_{\mathrm{cond}}/°\mathrm{C}$	61.2		61.7		62.0		61.5	
Evaporation pressure	$p_{\mathrm{eva}}/\mathrm{bar}$	2.87		0.42		0.50		0.63	
Intermediate pressure	$p_{\mathrm{int}}/\mathrm{bar}$	6.20		1.67		1.84		1.87	
Condensation pressure	$p_{\mathrm{cond}}/\mathrm{bar}$	17.4		4.22		4.80		5.53	
Fan electric power	$\dot{W}_{\mathrm{fan}}/\mathrm{kW}$	0.30		0.20		0.20		0.20	
Condenser									
Heat duty	$\dot{Q}_{\mathrm{cond}}/\mathrm{kW}$	17.3		17.1		17.3		17.0	
Weight	$\mathrm{weight}_{\mathrm{cond}}/\mathrm{kg}$	3.80		4.20		3.60		3.50	
Global dimensions	$W_{\mathrm{cond}} \times H_{\mathrm{cond}} \times D_{\mathrm{cond}}/\mathrm{m} \times \mathrm{m} \times \mathrm{m}$	0.78 × 0.20 × 0.02		0.60× 0.30 × 0.02		0.65× 0.23 × 0.02		0.77 × 0.18 × 0.02	
Air pressure drop	$\Delta p_{\mathrm{air,cond}}/\mathrm{kPa}$	0.31		0.19		0.20		0.20	
Air heat transfer coefficient	$h_{\mathrm{air,cond}}/\mathrm{W\ m^{-2}\ K^{-1}}$	308		195		253		241	
Air velocity	$v_{\mathrm{air,cond}}/\mathrm{m\ s^{-1}}$	6.30		5.50		6.50		6.85	
Refrigerant pressure drop	$\Delta p_{\mathrm{refr,cond}}/\mathrm{kPa}$	3.12		6.65		9.26		8.82	
Refrigerant heat transfer coefficient	$h_{\mathrm{refr,cond}}/\mathrm{W\ m^{-2}\ K^{-1}}$	2520		2405		3013		3112	
Refrigerant velocity	$v_{\mathrm{refr,cond}}/\mathrm{m\ s^{-1}}$	3.24		8.06		9.52		8.93	
Evaporator									
Weight	$\mathrm{weight}_{\mathrm{eva}}/\mathrm{kg}$	3.40		3.90		3.70		3.30	
Global dimensions	$W_{\mathrm{eva}} \times H_{\mathrm{eva}} \times D_{\mathrm{eva}}/\mathrm{m} \times \mathrm{m} \times \mathrm{m}$	0.50 × 0.43 × 0.06		0.32 × 0.54 × 0.06		0.30 × 0.64 × 0.06		0.36 × 0.49 × 0.06	
Air pressure drop	$\Delta p_{\mathrm{air,eva}}/\mathrm{Pa}$	190		228		208		227	
Air heat transfer coefficient	$h_{\mathrm{air,eva}}/\mathrm{W\ m^{-2}\ K^{-1}}$	125		132		128		133	
Air velocity	$v_{\mathrm{air,eva}}/\mathrm{m\ s^{-1}}$	2.50		3.0		2.70		3.0	
Refrigerant pressure drop	$\Delta p_{\mathrm{refr,eva}}/\mathrm{kPa}$	2.52		3.6		3.7		3.9	
Refrigerant heat transfer coefficient	$h_{\mathrm{refr,eva}}/\mathrm{W\ m^{-2}\ K^{-1}}$	2005		6111		5061		5085	
Refrigerant velocity	$v_{\mathrm{refr,eva}}/\mathrm{m\ s^{-1}}$	2.10		5.5		5.7		5.5	
Intercooler									
Heat duty	$\dot{Q}_{\mathrm{intcool}}/\mathrm{kW}$	3.80		1.50		1.30		1.70	
Weight	$\mathrm{weight}_{\mathrm{intcool}}/\mathrm{kg}$	1.90		2.20		0.80		0.95	
Twin-stage centrifugal compressor									
Centrifugal compressor power	$\dot{W}_{\mathrm{compr}}/\mathrm{kW}$	5.60		5.10		5.40		5.0	
Rotational speed	Ω/krpm	159		122		101		152	
Axial thrust	$F_{\mathrm{ax}}/\mathrm{N}$	24		18		11		8	
		1st stage	2nd stage	1st stage	2nd stage	1st stage	2nd stage	1st stage	2nd stage
Compression ratio	$\beta_{\mathrm{tt}}/–$	2.2	2.80	4.0	2.50	3.7	2.60	3.0	3.0
Total-to-total efficiency	$\eta_{\mathrm{tt}}/–$	0.79	0.70	0.82	0.81	0.82	0.80	0.83	0.80
Mass flow rate	$\dot{m}_{\mathrm{refr}}/\mathrm{kg\ s^{-1}}$	0.07	0.11	0.08	0.09	0.10	0.11	0.07	0.08
Swallowing capacity	$\Phi_{\mathrm{t1}}/–$	0.07	0.03	0.14	0.08	0.12	0.06	0.16	0.07
Loading coefficient	$\Psi/–$	0.67	0.71	0.70	0.71	0.69	0.70	0.65	0.70
Shape factor	$k/–$	0.85	0.76	0.95	0.84	0.90	0.86	0.94	0.84
Number of blades	$N_{\mathrm{bl}}/–$	13	16	15	18	18	18	20	20
Outlet absolute flow angle	$\alpha_2/°$	67.6	73.3	68.0	70.0	69.4	71.2	67.0	71.3
Outlet blade angle	$\beta_{2,\mathrm{bl}}/°$	−25.9	−33.1	−22.0	−27.5	−32.2	−32.3	−44.0	−39.3
Inlet impeller radius at hub	$R_{1,\mathrm{hub}}/\mathrm{mm}$	2.50	2.90	3.06	3.52	4.15	3.46	2.54	3.05
Outlet blade height	H_2/mm	1.25	0.68	2.63	1.68	2.70	1.54	2.96	1.47
Diffuser to outlet impeller radii ratio	$R_3/R_2/–$	1.40	1.35	1.48	1.32	1.47	1.43	1.76	1.38
Inlet relative Mach at shroud	$M_{\mathrm{w}_{1,\mathrm{s}}}/–$	0.78	0.71	1.29	0.85	1.20	0.80	1.25	0.92

[a] The temperature at the outlet of the evaporator is imposed equal to 0 °C for all the working fluids. The effect of the pressure drop generates a temperature glide and a consequent increase of the temperature at the evaporator inlet.

The nadir point is the worst value for each objective function in the design space

$$\hat{z}_q^{\mathrm{N}} = \max\{f_q(x) \mid x \in \Omega\}. \tag{11}$$

Afterwards, the ASF decomposition method is applied. Its mathematical expression is

$$\min\left\{g^{\mathrm{ASF}}(x \mid w, z^*) = \max\left\{\frac{1}{w_i} \mid f_i(x) - z_i^* \mid\right\}\right\} \tag{12}$$

Here, the same weight has been assigned to both objective functions, since they are assumed to be equally important for the definition of the best design point. Table 9 reports a list of the main system design parameters, corresponding to the optimal points forming the Pareto front associated with each refrigerant.

In the case of haloolefins as working fluids, the corresponding optimal designs are similar, due to the comparable thermodynamic properties of these refrigerants. The optimal operating temperature levels are the same. With respect to the temperature in the evaporator, since the outlet flow temperature is fixed and set equal to 0 °C, any difference in the flow temperature at the inlet is due to the effect of the temperature glide associated with the pressure drop, which is always higher in the case of haloolefins with respect to R-134a. For the same levels of operating temperature, the corresponding saturation pressures are inherently lower as compared to the benchmark fluid. In particular, the use of haloolefins implies evaporators operating at sub-atmospheric pressures, which poses some technological challenges associated with their mechanical design. The optimal system designs obtained if haloolefins are the working fluids allow to achieve higher

COP with respect to those for which R-134a is the working fluid. In particular, R-1234ze(Z) would allow to achieve the best thermodynamic performance and a lower weight if compared to those calculated for the benchmark case, with a COP that is 9% higher and a weight that is almost 10% lower. The fan electric power demand does not vary depending on the working fluid of the system, hence, the difference in system efficiency can only be associated with the electric power needed to drive the compressor, which is 10% lower in case R-1234ze(Z) is the working fluid, since the required refrigerant mass flow rate is lower. At the same time, the design of the twin-stage centrifugal compressor is very compact and features a high rotational speed, in excess of 150 krpm. With respect to the designs obtained for the other two haloolefins, due to the combination of a lower overall pressure ratio and power demand and low flow density, the impeller wheel diameters are smaller and the flow passages are larger.

7. Conclusions and future works

The effect of the working fluid on the optimal design of a novel concept of environmental control system aboard helicopters has been analysed. The proposed system is based on the vapour compression cycle principle and adopts as the prime mover a small-scale high-speed centrifugal compressor in place of the traditional scroll compressor. The considered working fluids are R-1233zd(E), R-1234ze(Z), R-1224yd(Z) and R-1336mzz(Z). These refrigerants are haloolefins, and they are likely to become next-generation refrigerants, thanks to their low global warming potential. The benchmark case is the optimal system for which the state-of-the-art refrigerant R-134a is the working fluid. Steady-state and lumped parameter models of the main system components have been developed resorting to the acausal Modelica modelling language. An optimization framework has been coded to integrate the in-house compressor design tool *TurboSim* within the Modelica system model, using Python. Such a method allows for the system cycle calculations, simultaneously calculating the preliminary design of the system components. A multi-objective optimization has been performed using a gradient-free algorithm. The objective functions are maximum system COP and minimum system weight. The case study is the ECS of a large passenger helicopter. The optimization has been conducted for a critical operating point of the system: the helicopter is on the ground on a hot and humid day.

The main conclusions derived from this work are summarized as follows:

(i) A Pareto front of optimal design solutions is obtained for all the working fluids, except for R-1336mzz(Z). The results show that system efficiency can only be enhanced at the expense of heavier heat transfer equipment.

(ii) High efficiency system designs, featuring lightweight components are possible also with haloolefins as working fluids. Among these fluids, R-1234ze(Z) is identified as the best replacement for R-134a, allowing to obtain a maximum COP increase equal to 12% and a maximum weight reduction of 26%. However, the mild flammability of this refrigerant complicates system certification.

(iii) The adoption of haloolefins as working fluids results in heavier evaporators. The low vapour density of these refrigerants leads to designs featuring a large number of minichannels, so that the flow velocity, and hence the associated friction losses can be kept within acceptable values.

(iv) The condenser is the heaviest component among the heat exchangers installed in the system. Its weight increases with the system COP, within a range from 3 kg to 6 kg. This trend is independent of the refrigerant choice. The optimal condenser designs feature large flow passages on the air stream to limit the ram air pressure drop, hence the associated fan electric power consumption.

(v) The design of a twin-stage high-speed centrifugal compressor is feasible. The use of haloolefins allows for compressor efficiency of up to 80%. Thanks to the low vapour density of these refrigerants, larger flow passages and impeller wheel radii can be obtained, overcoming the challenges associated with small-capacity centrifugal compressor manufacturability. Despite the limited size of the compressor, the rotational speed never exceeds a maximum of 160 krpm. Gas bearings can be used for the rotor since the net axial thrust never exceeds 26 N.

(vi) R-1336mzz(Z) is not suitable for the considered application. Because of its high molecular complexity, the flow speed of sound at the suction port of the compressor is inherently low. This makes the thermo-fluid dynamic design of the compressor challenging because of the losses associated with secondary flows and mixing due to shock interaction within the rotor flow channels. Furthermore, a safe operation of the compressor would be challenging, since the design mass flow rate is close to the choking.

The analysis of the VCC-based Environmental Control System operation in off-design conditions may lead to different results as far as the selection of the working fluids is concerned. Therefore, future work will address the multi-point optimization of the Environmental Control System of a rotorcraft over its flight envelope, while simultaneously accounting for the selection of the working fluid used in the VCC system.

CRediT authorship contribution statement

F. Ascione: Writing – original draft, Validation, Software, Methodology, Data curation, Conceptualization. **A. Giuffré:** Writing – review & editing, Software, Methodology, Conceptualization. **P. Colonna:** Writing – review & editing, Supervision, Funding acquisition. **C.M. De Servi:** Writing – review & editing, Supervision, Funding acquisition, Conceptualization.

Declaration of competing interest

The authors declare that they have no known competing financial interests or personal relationships that could have appeared to influence the work reported in this paper.

Acknowledgements

The authors gratefully acknowledge the contribution of Dr. Vincent Pommé of Airbus Helicopters for the continued support and for providing suggestions and information regarding the selection of the design point and of the VCC system configuration. This research is supported by Aeronamic BV, by the Applied and Engineering Sciences Division (TTW) of the Dutch Organization for Scientific Research (NWO) via the Technology Program of the Ministry of Economic Affairs of the Netherlands (Grant No. 17091).

Appendix

List of the constant parameters chosen for the design of the evaporator, the condenser, and the intercooler, in accordance with the guidelines by Ascione et al. (2024) (Table 10).

Table 10
Design values assigned to the geometry of multi-louvered fins and minichannels within condenser and evaporator, and of the flat plate chevron type HEX used as intercooler. These data have been chosen equal to those selected by Ascione et al. (2024).

Evaporator		
Geometrical parameter	Symbol	Value
Tube height	T_h/mm	2
Tube wall thickness	δ_t/mm	0.4
Tubes pitch	T_p/mm	9.4
Number of minichannels	N_mc/–	16
Minichannels wall thickness	δ_mc/mm	0.35
Fins pitch	F_p/mm	3
Fins thickness	δ_f/mm	0.12
Condenser		
Geometrical parameter	Symbol	Value
Tube height	T_h/mm	1.93
Tube wall thickness	δ_t/mm	0.4
Tubes pitch	T_p/mm	2.33
Number of minichannels	N_mc/–	12
Minichannels wall thickness	δ_mc/mm	0.3
Fins pitch	F_p/mm	1.4
Fins thickness	δ_f/mm	0.115
Intercooler		
Geometrical parameter	Symbol	Value
Number of passes (both refrigerant streams)	N_pass	1
Number of channels per pass (both refrigerant streams)	N_channel/–	40
Flat plate width	W_plate/mm	120
Port diameter	D_port/mm	30
Amplitude sinusoidal corrugation pattern	Λ/mm	1.5
Wave length corrugation pattern	a/mm	10
Flat plate thickness	δ_plate/mm	0.4
Plate inclination angle	β_plate/°	60

References

AIR1168/8, 2011. Aircraft fuel weight penalty due to air conditioning. SAE Int. (AC-9 Aircraft Environmental Systems Committee), 20. http://dx.doi.org/10.4271/AIR1168/8A.

Andersen, M.P.S., Schmidt, J.A., Volkova, A., Wuebbles, D.J., 2018. A three-dimensional model of the atmospheric chemistry of E and Z-CF3CH=CHCl (HCFO-1233 (zd)(E/Z)). Atmos. Environ. 179, 250–259. http://dx.doi.org/10.1016/j.atmosenv.2018.02.018.

Angelino, G., Invernizzi, C., 1988. General method for the thermodynamic evaluation of heat pump working fluids. Int. J. Refrig. 11 (1), 16–25. http://dx.doi.org/10.1016/0140-7007(88)90007-2.

ANSI/ASHRAE Standard 34, 2022. ASHRAE Standard 34-2022 - Designation and Safety Classification of Refrigerants.

ARP292, 2014. Air conditioning helicopter general requirements. (AC-9 Aircraft Environmental Systems Committee), p. 7. http://dx.doi.org/10.4271/ARP292,

Arpagaus, C., Bertsch, S., 2021. Experimental comparison of HCFO and HFO R-1224yd(Z), R-1233zd(E), R-1336mzz(Z), and HFC R-245fa in a high temperature heat pump up to 150 °C supply temperature. In: 18th International Refrigeration and Air Conditioning Conference. Purdue University, p. 13.

Arpagaus, C., Kuster, R., Prinzing, M., Bless, F., Uhlmann, M., Büchel, E., Frei, S., Schiffmann, J., Bertsch, S.S., 2019. High temperature heat pump using HFO and HCFO refrigerants-System design and experimental results. In: Refrigeration Science and Technology Proceedings. 25th IIR International Congress of Refrigeration. pp. 4239–4247.

Ascione, F., Colonna, P., De Servi, C.M., 2024. Integrated design optimization method for novel vapour-compression-cycle-based environmental control systems. Appl. Therm. Eng. 236, 121261. http://dx.doi.org/10.1016/j.applthermaleng.2023.121261.

Ascione, F., De Servi, C.M., Meijer, O., Pommé, V., Colonna, P., 2021. Assessment of an Inverse Organic Rankine Cycle system for the ECS of a large rotorcraft adopting a high-speed centrifugal compressor and a low GWP refrigerant. In: of Munich, T.U. (Ed.), Proceedings of the 6th International Seminar on ORC Power Systems. Technical University of Munich, Munich, Germany, p. 10. http://dx.doi.org/10.14459/2021mp1633127.

Aspen Technology, 2008. Aspen exchanger design & rating - Applying Aspen HTFS technology.

Bendapudi, S., Braun, J.E., Groll, E.A., 2008. A comparison of moving-boundary and finite-volume formulations for transients in centrifugal chillers. Int. J. Refrig. 31 (8), 1437–1452. http://dx.doi.org/10.1016/j.ijrefrig.2008.03.006.

Bender, D., 2019. Exergy-Based Analysis of Aircraft Environmental Control Systems and its Integration into Model-Based Design (Ph.D. thesis). Technischen Universität Berlin, Berlin.

Blank, J., Deb, K., 2020. Pymoo: Multi-objective optimization in Python. IEEE Access 8, 89497–89509. http://dx.doi.org/10.1109/ACCESS.2020.2990567.

Buticchi, G., Wheeler, P., Boroyevich, D., 2022. The more-electric aircraft and beyond. Proc. IEEE 1–15. http://dx.doi.org/10.1109/JPROC.2022.3152995.

Chang, Y.-J., Wang, C.-C., 1997. A generalized heat transfer correlation for louver fin geometry. Int. J. Heat Mass Transfer 40 (3), 533–544. http://dx.doi.org/10.1016/0017-9310(96)00116-0.

Cooper, M., 1984. Heat flow rates in saturated nucleate pool boiling-a wide-ranging examination using reduced properties. In: Advances in Heat Transfer, vol. 16, Elsevier, pp. 157–239.

EASA CS-25.863, 2016. Certification Specifications for Large Aeroplanes. Technical Report ED Decision 2016/010/R, European Union Aviation Safety Agency (EASA), CS 25.863 Flammable Fluid Fire Protection.

ECHA, E., 2023. Annex XV Restriction Report. Proposal for a Restriction. Per-and Polyfluoroalkyl Substances (PFASs). European Chemicals Agency, Helsinki.

Eckardt, D., 1975. Instantaneous measurements in the jet-wake discharge flow of a centrifugal compressor impeller. J. Eng. Gas Turbines Power 97 (3), 337–345. http://dx.doi.org/10.1115/1.3445999.

Eckardt, D., 1976. Detailed flow investigations within a high-speed centrifugal compressor impeller. J. Fluids Eng. Trans. ASME 98 (3), 390–399. http://dx.doi.org/10.1115/1.3448334.

Eckardt, D., 1977. Investigation of the Jet-Wake Flow of a Highly-Loaded Centrifugal Compressor Impeller (Ph.D. thesis). Rheln Westfael Technical School, Aachen, West Germany, pp. 1–227.

European Commission, 2011. Flightpath 2050 Europe's Vision for Aviation: Maintaining Global Leadership and Serving Society's Needs. Technical Report, Publications Office, LU.

European Commission, 2022. Proposal for a regulation of the european parliament and of the council on fluorinated greenhouse gases, amending Directive (EU) 2019/1937 and repealing Regulation (EU) No 517/2014.

Friedel, L., 1979. Improved friction pressure drop correlations for horizontal and vertical two-phase pipe flow. In: European Two-Phase Group Meeting, Ispra, Italy.

Giuffré, A., Ascione, F., Servi, C.D., Pini, M., 2023. Data-driven modeling of high-speed centrifugal compressors for aircraft Environmental Control Systems. Int. J. Refrig. http://dx.doi.org/10.1016/j.ijrefrig.2023.03.019.

Giuffré, A., Colonna, P., Pini, M., 2022a. Design optimization of a high-speed twin-stage compressor for next-gen aircraft environmental control system. J. Eng. Gas Turbines Power 145 (3), http://dx.doi.org/10.1115/1.4056022.

Giuffré, A., Colonna, P., Pini, M., 2022b. The effect of size and working fluid on the multi-objective design of high-speed centrifugal compressors. Int. J. Refrig. 143, 43–56. http://dx.doi.org/10.1016/j.ijrefrig.2022.06.023.

Gnielinski, V., 2013. On heat transfer in tubes. Int. J. Heat Mass Transfer 63, 134–140. http://dx.doi.org/10.1016/j.ijheatmasstransfer.2013.04.015.

Heath, E.A., 2017. Amendment to the Montreal protocol on substances that deplete the ozone layer (Kigali amendment). Int. Leg. Mater. 56 (1), 193–205. http://dx.doi.org/10.1017/ilm.2016.2.

Hodnebrog, Ø., Aamaas, B., Fuglestvedt, J.S., Marston, G., Myhre, G., Nielsen, C.J., Sandstad, M., Shine, K.P., Wallington, T.J., 2020. Updated global warming potentials and radiative efficiencies of halocarbons and other weak atmospheric absorbers. Rev. Geophys. 58 (3), http://dx.doi.org/10.1029/2019RG000691.

Hundy, G.F., Trott, A.R., Welch, T.C., 2016. Refrigeration, Air Conditioning and Heat Pumps. Butterworth-Heinemann.

IEC 60335-2-40:2022, 2022. Household and Similar Electrical Appliances - Safety - Part 2-40: Particular Requirements for Electrical Heat Pumps, Air-Conditioners and Dehumidifiers. Technical Report.

IEC 60335-2-89:2019, 2023. Household and Similar Electrical Appliances - Safety - Part 2-89: Particular Requirements for Commercial Refrigerating Appliances and Ice-Makers with an Incorporated or Remote Refrigerant Unit or Motor-Compressor. Technical Report.

Invernizzi, C.M., 2013. Closed Power Cycles: Thermodynamic Fundamentals and Applications. In: Lecture Notes in Energy, vol. 11, Springer London, London, http://dx.doi.org/10.1007/978-1-4471-5140-1.

Japikse, D., 1987. A critical evaluation of three centrifugal compressors with pedigree data sets: Part 5-studies in component performance. J. Turbomach. 109 (1), 1–9. http://dx.doi.org/10.1115/1.3262064.

Kandlikar, S.G., 1990. A general correlation for saturated two-phase flow boiling heat transfer inside horizontal and vertical tubes. J. Heat Transf. 112 (1), 219–228. http://dx.doi.org/10.1115/1.2910348.

Kast, W., Nirschl, H., Gaddis, E.S., Wirth, K.E., Stichlmair, J., 2010. L1 - Pressure drop in single phase flow. In: VDI Heat Atlas. Springer Berlin Heidelberg, Berlin, Heidelberg, pp. 1053–1116. http://dx.doi.org/10.1007/978-3-540-77877-6.

Kim, M.-H., Bullard, C.W., 2002. Air-side thermal hydraulic performance of multi-louvered fin aluminum heat exchangers. Int. J. Refrig. 25 (3), 390–400. http://dx.doi.org/10.1016/S0140-7007(01)00025-1.

Kim, M.-H., Bullard, C.W., 2022. Performance evaluation of a window room air conditioner with microchannel condensers. J. Energy Resour. Technol. 124(1): 47-55, 9. http://dx.doi.org/10.1115/1.1446072.

Lemmon, E.W., Bell, I.H., Huber, M.L., McLinden, M.O., 2018. NIST Standard Reference Database 23: Reference Fluid Thermodynamic and Transport Properties-REFPROP, Version 10.0. National Institute of Standards and Technology.

Lockhart, R.W., 1949. Proposed correlation of data for isothermal two-phase, two-component flow in pipes. Chem. Eng. Prog. 45, 39–48.

Mannini, A., 1995. The environmental control system for a modern helicopter: A blend of new technologies. In: Twenty-First European Rotorcraft Forum. Saint-Petersburg, Russia, p. 11.

Martin, H., 1996. A theoretical approach to predict the performance of chevron-type plate heat exchangers. Chem. Eng. Process. 35, 10. http://dx.doi.org/10.1016/0255-2701(95)04129-X.

McLinden, M.O., Seeton, C.J., Pearson, A., 2020. New refrigerants and system configurations for vapor-compression refrigeration. Science 370 (6518), 791–796. http://dx.doi.org/10.1126/science.abe3692.

MIL-STD-882E, 2023. Department of Defense Standard Practice – System Safety. Technical Report MIL-STD-882E Change 1, United States Department of Defense, Originally issued May 11, 2012; Change 1 issued September 27, 2023.

Modelica Association, 2021. Modelica Language Specification, Version 3.5. Technical Report, Modelica Association.

Mohanraj, M., Abraham, J.D.A.P., 2022. Environment friendly refrigerant options for automobile air conditioners: a review. J. Therm. Anal. Calorim. 147 (1), 47–72. http://dx.doi.org/10.1007/s10973-020-10286-w.

Molés, F., Navarro-Esbrí, J., Peris, B., Mota-Babiloni, A., Barragán-Cervera, A., 2014. Theoretical energy performance evaluation of different single stage vapour compression refrigeration configurations using R1234yf and R1234ze(E) as working fluids. Int. J. Refrig. 44, 141–150. http://dx.doi.org/10.1016/j.ijrefrig.2014.04.025.

Prabakaran, R., Lal, D.M., Kim, S.C., 2023. A state of art review on future low global warming potential refrigerants and performance augmentation methods for vapour compression based mobile air conditioning system. J. Therm. Anal. Calorim. 148 (2), 417–449. http://dx.doi.org/10.1007/s10973-022-11485-3.

Rusch, D., Casey, M., 2013. The design space boundaries for high flow capacity centrifugal compressors. J. Turbomach. 135 (3), 031035. http://dx.doi.org/10.1115/1.4007548.

Schiffmann, J., Favrat, D., 2009. Experimental investigation of a direct driven radial compressor for domestic heat pumps. Int. J. Refrig. 32 (8), 1918–1928. http://dx.doi.org/10.1016/j.ijrefrig.2009.07.006.

Schiffmann, J., Favrat, D., 2010. Design, experimental investigation and multi-objective optimization of a small-scale radial compressor for heat pump applications. Energy 35 (1), 436–450. http://dx.doi.org/10.1016/j.energy.2009.10.010.

Shah, M.M., 2019. Improved correlation for heat transfer during condensation in conventional and mini/micro channels. Int. J. Refrig. 98, 222–237. http://dx.doi.org/10.1016/j.ijrefrig.2018.07.037.

Shah, R.K., Sekulić, D.P., 2003. Heat exchanger surface geometrical characteristics. In: Fundamentals of Heat Exchanger Design. John Wiley & Sons, Ltd, pp. 563–600. http://dx.doi.org/10.1002/9780470172605.ch8, chapter 8.

Stanitz, J., 1952. One-Dimensional Compressible Flow in Vaneless Diffusers of Radial-And Mixed-Flow Centrifugal Compressors, Including Effects of Friction, Heat Transfer and Area Change. Technical Report, National Advisory Committee for Aeronautics.

Tiainen, J., Jaatinen-Värri, A., Grönman, A., Sallinen, P., Honkatukia, J., Hartikainen, T., 2021. Validation of the axial thrust estimation method for radial turbomachines. Int. J. Rotating Mach. 2021, http://dx.doi.org/10.1155/2021/6669193.

Urbańczyk, A., Wright, J., Cowden, D., Solutions, I.T., ÖZDERYA, H.Y., Agostini, B., Greminger, M., Buchanan, J., huskier, Boyd, M., de León Peque, M.S., Boin, P., Weissinger, B., Osterwood, C., moeb, nopria, Kono, A., HLevering, Turner, W., Saville, W., Grunichev, A., Bernhard, Anderson, D., Ebner, G., Krasin, I., Ulianko, M., Thelen, P., bsilvereagle, jwhevans, xix xeaon, 2020. Cadquery/cadquery 2.0.1. http://dx.doi.org/10.5281/zenodo.3955119.

Van Der Geest, M., Polinder, H., Ferreira, J.A., Christmann, M., 2015. Power density limits and design trends of high-speed permanent magnet synchronous machines. IEEE Trans. Transp. Electrification 1 (3), 266–276. http://dx.doi.org/10.1109/TTE.2015.2475751.

Wierzbicki, A.P., 1982. A mathematical basis for satisficing decision making. Math. Model. 3 (5), 391–405. http://dx.doi.org/10.1016/0270-0255(82)90038-0.

Yataganbaba, A., Kilicarslan, A., Kurtbaş, I., 2015. Exergy analysis of R1234yf and R1234ze as R134a replacements in a two evaporator vapour compression refrigeration system. Int. J. Refrig. 60, 26–37. http://dx.doi.org/10.1016/j.ijrefrig.2015.08.010.

Zaporozhets, O., Isaienko, V., Synylo, K., 2021. PARE preliminary analysis of ACARE FlightPath 2050 environmental impact goals. CEAS Aeronaut. J. 12 (3), 653–667. http://dx.doi.org/10.1007/s13272-021-00525-7.

Zohuri, B., 2017. Compact Heat Exchangers. Springer International Publishing, Cham, http://dx.doi.org/10.1007/978-3-319-29835-1.